AGU PUBLICATIONS

JGR

Journal of Geophysical Research: Solid Earth

RESEARCH ARTICLE
10.1002/2016JB012934

Key Points:
- We present a method for jointly inverting noise and teleseismic surface wave data for phase velocity maps
- Joint inversion improves model recovery inside and outside of the array
- New phase velocity maps image low-velocity regions in Iceland associated with rifting and seafloor spreading

Supporting Information:
- Supporting Information S1

Correspondence to:
N. Harmon,
n.harmon@soton.ac.uk

Citation:
Harmon, N., and C. A. Rychert (2016), Joint inversion of teleseismic and ambient noise Rayleigh waves for phase velocity maps, an application to Iceland, *J. Geophys. Res. Solid Earth*, *121*, 5966–5987, doi:10.1002/2016JB012934.

Received 17 FEB 2016
Accepted 5 AUG 2016
Accepted article online 6 AUG 2016
Published online 25 AUG 2016

Joint inversion of teleseismic and ambient noise Rayleigh waves for phase velocity maps, an application to Iceland

Nicholas Harmon[1] and Catherine A. Rychert[1]

[1]National Oceanography Centre, University of Southampton, Southampton, UK

Abstract We present a method for joint inversion of teleseismic and ambient noise Rayleigh wave data for phase velocity maps from 18 to 50 s period. We adapt the two-plane wave method for teleseismic data to include ambient noise phase data. We apply the method to data from Iceland's ICEMELT and HOTSPOT arrays. Checkerboard tests show that the joint inversion improves phase velocity model recovery over methods that use the data sets independently, particularly at 18 s period. The addition of ambient noise data also extends resolution to shallower depths and shorter periods in comparison to previous teleseismic results beneath Iceland. We show there are significant differences in the phase velocity maps from the joint approach in comparison to other approaches, for instance, using only teleseismic data, only ambient noise data, or the mean of the two. The difference in phase velocities in turn affects the resulting shear velocity models. The advantage of the joint inversion is that it produces a single phase velocity map that satisfies both data sets simultaneously. Our phase velocity maps show a transition from low velocities centered beneath the main volcanic centers in Iceland at 18–25 s period, primarily crustal depths, to a low-velocity region that traces the rift zones from the Reykjanes Ridge in the south to the Kolbeinsey Ridge in the north at 29–50 s period, greater depths. These results are consistent with previous studies, although with an extended and improved region of resolution, which extends further into the Atlantic and Arctic Ocean.

1. Introduction

The development of array-based methods for teleseismic surface wave tomography [*Forsyth and Li*, 2005; *Lin and Ritzwoller*, 2011; *Pollitz and Snoke*, 2010] and ambient noise tomography [e.g., *Sabra et al.,* 2005; *Shapiro et al.,* 2005] has improved the resolution of regional seismic velocity models. Array-based methods model the incoming wavefield for a teleseismic event along with changes in velocity using observations from an array of stations [*Forsyth and Li*, 2005; *Lin and Ritzwoller*, 2011; *Pollitz and Snoke*, 2010], compared to single station or two station methods [e.g., *Aki and Richards*, 2002]. These methods are effective with a sufficient array aperture, wide enough to sample the longest wavelengths of interest and also a station spacing smaller than half the shortest wavelength of interest to avoid aliasing. These methods have been shown to be very successful for imaging both inside and outside of the array where event raypaths cross, using periods as short at 16 s and routinely up to 143 s period [*Harmon et al.,* 2009; *Weeraratne et al.,* 2007; *Yang et al.,* 2007]. Given a uniform station spacing, array-based methods can be used to estimate gradients of the observed wavefield, which can be used for Eikonal/Helmholtz tomography [e.g., *Liang and Langston*, 2009; *Lin and Ritzwoller*, 2011]. The disadvantage of these methods is that both a good back azimuthal event distribution and an appropriate station geometry (described above) are required. In addition, measurements of dispersion at the shortest periods (<30 s) can be limited by wavefield complications such as multipathing and scattering, source characteristics, and attenuation. Typically, there are large numbers of useable events from 33 to 50 s period, with decreasing numbers at shorter and longer periods [*Harmon et al.,* 2009; *Weeraratne et al.,* 2007; *Yang et al.,* 2007].

Ambient noise tomography (ANT) uses empirical Green's functions from ambient noise cross correlation between station pairs to estimate velocity variations within a seismic array. Cross correlation and stacking of seismic records between stations produces empirical Green's functions (EGF) for surface waves traveling between the two seismic stations [*Shapiro and Campillo*, 2004]. The amplitudes and travel times of the EGF can be used to estimate surface wave velocities to very short periods (<1–10 s) and are routinely used to invert for phase, group, and/or shear velocity structure within a seismic array [e.g., *Sabra et al.,* 2005; *Shapiro et al.,* 2005]. Typically, for a broadband seismic array with tens of kilometers station spacing,

dispersion measurements can be made down to 5–6 s period [*Shapiro and Campillo*, 2004; *Shapiro et al.,* 2005] and up to a 200 s globally [*Schimmel et al.,* 2011]. High spatial density (approximately meter scale), short-period seismic arrays have recovered dispersion measurements down to ~1 s [*Mordret et al.,* 2013]. For a given regional array, the longest period useable for tomography is dependent on the noise characteristics of the ambient noise sources and the interstation distance. The latter is a limiting factor because the far field approximation typically employed for estimating group and phase velocities is only accurate at >2–3 times the seismic wavelength for the station spacing [*Harmon et al.,* 2010], but this condition can be relaxed if better approximations are used [*Luo et al.,* 2015]. Therefore, as the period increases typically, there are fewer station pairs that satisfy the station spacing criteria and fewer data available for tomography.

Typically, ambient noise and teleseismic data are inverted for phase velocity maps independently and the phase velocity maps are then jointly inverted for shear velocity structure [*Harmon et al.,* 2007, 2013; *Ma and Clayton*, 2014; *Yang et al.,* 2008]. A period range is chosen where one or the other method's phase velocity estimates will be used and/or where they overlap the results are averaged [*Zhou et al.,* 2012]. This approach has enhanced the shear velocity models as dispersion can be estimated from a few seconds to > 100 s, which allows for better constraints on crustal structure from the short-period dispersion with fewer prior assumptions. This prevents mapping of crustal velocity anomalies into upper mantle structure. However, in the period range where teleseismic and ambient noise overlap, only one inversion scheme has directly combined the two data types [*Porritt et al.,* 2014] to invert for a phase velocity map that satisfies both data sets simultaneously. The inversion used a multiple plane wave parameterization for the teleseismic inversion [*Pollitz and Snoke*, 2010].

In this paper we present a method for combining teleseismic and ambient noise data to invert for phase velocity maps. We use the two-plane wave tomographic method with 2-D finite-frequency sensitivity kernels [*Forsyth and Li*, 2005; *Yang and Forsyth*, 2006] for teleseismic data and use a consistent parameterization for ambient noise data for the joint inversion. The advantage of the joint inversion is that ambient noise can constrain the structure inside the array and aid the resolution of the crossing teleseismic raypaths outside the array. We demonstrate the utility of this approach using data from the ICEMELT and HOTSPOT arrays in Iceland (Figures 1 and 2a).

1.1. Previous Geophysical Work on Iceland

Iceland is the archetype example of plume-ridge interaction where melt production at a mid-ocean ridge is enhanced by a focused mantle upwelling [*Morgan*, 1971; *Wilson*, 1965]. It is one of the largest subaerial large igneous provinces on Earth located on the slow-spreading Mid-Atlantic Ridge [*Coffin and Eldholm*, 1994]. It is associated with a broad topographic swell [*Vogt*, 1976], suggesting that it is being uplifted by buoyant mantle material with melting enhanced beneath the ridge by a hot plume. Geochemical changes along the Mid-Atlantic Ridge going onshore to Iceland also suggest a change from mid-ocean ridge-type mantle melting to higher-temperature-enriched mantle melting beneath Iceland [*Schilling*, 1973]. The location of the plume at depth has also been linked to the eastward migration of the rift system on Iceland, evidenced by jumps in ages of the rocks in western Iceland [*Martin et al.,* 2011; *Saemundsson*, 1974]. However, the exact relationship between the plume and rift system and the nature of the plume is still an active area of research.

Iceland's crustal structure has been well characterized geophysically. Crustal structure has been estimated using *S*-to-*P* and *P*-to-*S* receiver functions and active source seismic studies combined with gravity [*Darbyshire et al.,* 2000; *Kumar et al.,* 2007]. Thickened crust up to 45 km is present near the intersection of the Northern and Eastern Volcanic Zones and beneath the NW Fjords, with typical crustal values of 20–30 km elsewhere. Thinner crust is associated with the Western and Northern Volcanic Zones [*Allen et al.,* 2002b; *Darbyshire et al.,* 2000; *Kumar et al.,* 2007].

The crust and upper most mantle, <200 km depth, has been characterized by previous surface wave studies which find a low-velocity region centered on Iceland [*Allen et al.,* 2002a; *Li and Detrick,* 2004, 2006]. The shallowest low-velocity anomalies are associated with thickened crust (<50 km). There is a fast lid present in the upper 60–80 km visible across Iceland, which appears to thin or become slower beneath the Western and Northern Volcanic Zones [*Li and Detrick,* 2004, 2006]. There is a low-velocity zone from 80 to 120 km depth across the region, with the lowest velocity focused near the Volcanic Zones [*Li and Detrick,* 2004, 2006]. These results are generally consistent with a thickening conductively cooling lid away from the rift, with

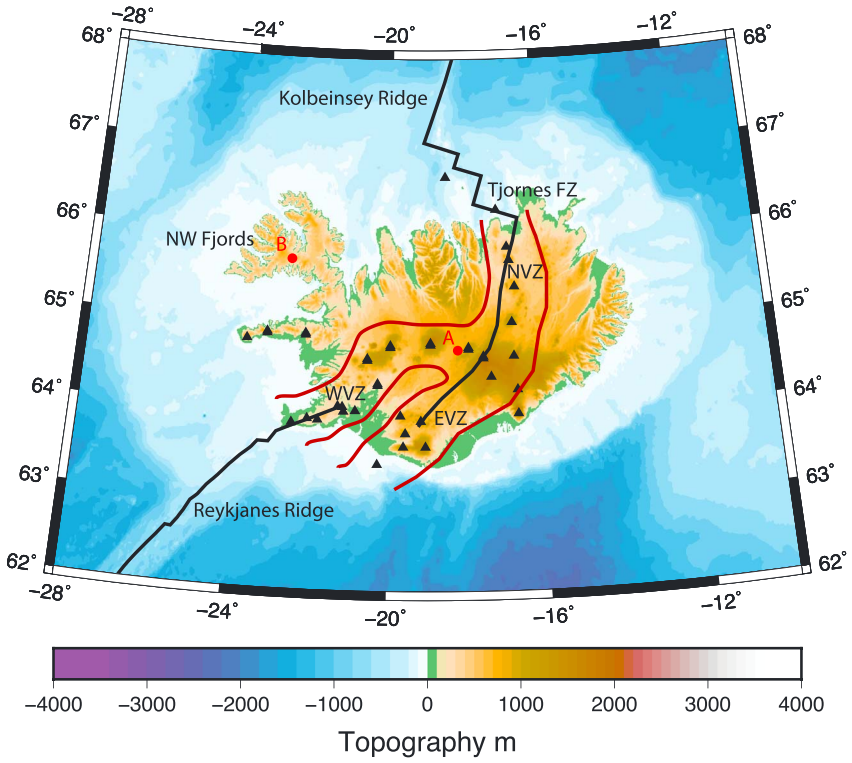

Figure 1. Iceland Topography highlighting tectonic features. The black line shows the plate boundary model of *Bird* [2003]. Black triangles show the locations of volcanoes active during the Holocene [*Venzke*, 2013], and the red lines indicate the lateral extent of Quaternary volcanics in the rift regions of Iceland [*Asch*, 2003]. The black triangles and red lines are included in subsequent figures for reference. Locations and features are labeled on the map, WVZ = Western Volcanic Zone, EVZ = Eastern Volcanic Zone and NVZ = Northern Volcanic Zone, and Tjornes FZ = Tjornes Fracture Zone. Points A and B are the locations for the representative dispersion curves and shear velocity models presented later in the text.

lateral spreading of hotter asthenospheric material. A high-velocity anomaly centered at 135 km depth beneath the intersection of the Volcanic Zones has been interpreted either as being due to a depleted mantle residual caused by melt extraction or an anisotropic effect from upwelling mantle material [*Li and Detrick,* 2004, 2006].

Many body wave tomography studies have imaged a 200 km diameter cylindrical shaped low-velocity region beneath the intersection of the Volcanic Zones that extends from the Moho to the mantle transition zone [*Allen et al.,* 2002a; *Foulger et al.,* 2000; *Wolfe et al.,* 1997]. This low-velocity region has been interpreted as the plume conduit. There is some debate as to whether these anomalies and the mantle plume extend deeper [*Foulger et al.,* 2000], but there is some evidence that the plume may extend deeper based on topography of the 410 and 660 discontinuities [*Shen et al.,* 1998].

2. Methods

2.1. Data Processing of Ambient Noise

Continuous vertical component broadband seismic data from the HOTSPOT experiment in Iceland [*Allen et al.,* 1999], including station BORG, were used for the ambient noise tomography (Figure 2a). Seismic records sampled at 1 Hz were processed for each day. We removed the instrument response, then we preprocessed the data for cross correlation by normalizing the amplitudes using a running mean of the RMS of the signal in a 100 s window and spectrally whitening prior to cross correlation from 0.01 to 0.33 Hz [*Bensen et al.,* 2007]. Cross correlations for all possible days were stacked to generate the noise cross-correlation functions (NCF) (Figure 2b).

To estimate the phase for each station pair and frequency of interest, we used the causal, symmetric part of the signal, which should minimize phase shifts due to inhomogeneous noise distribution [*Harmon et al.,*

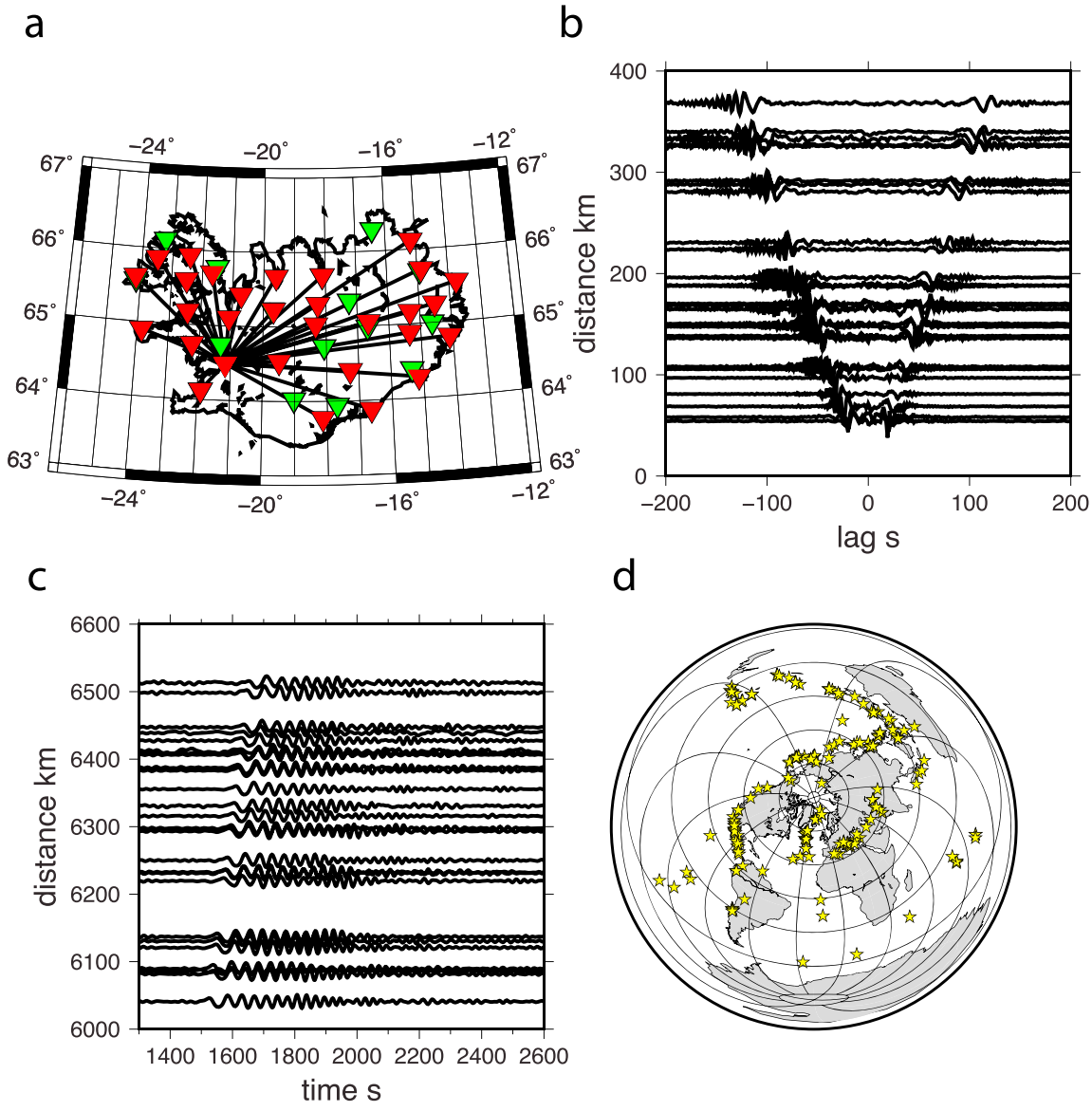

Figure 2. Data Examples. (a) Map showing stations used in the teleseismic study (red and green triangles) and ANT (red triangles). Black lines show station-to-station paths, for example, NCF. (b) Example NCF sorted by interstation distance. (c) Example teleseismic seismograms for event on 30 May 1998 ordered as a function of epicentral distance. (d) Teleseismic earthquakes (yellow stars) used in this study.

2010]. The NCF were visually inspected, and records with no clear signal, i.e., signal-to-noise ratio < 3 or complicated signals, were discarded. The causal, symmetric NCF was windowed using a Tukey window with a 50 s falloff, with the falloff set at the predicted group arrival times at 5 km/s $-$ 50 s and 2 km/s + 50 s. The windowed NCF were then Fourier transformed and the phase determined. At each frequency of interest we determine the cycle ambiguity for each station-to-station NCF by unwrapping the phase in the spatial domain until the phase clustered around a single line (within $\pm\pi$) as a function of distance. Unwrapping can be performed by sorting the data by distance and then checking for jumps $> \pi$, and no prior information about velocity structure is required. This is similar to techniques that use beamforming or wave number estimates to estimate the mean phase velocity across an array [*Harmon et al.,* 2008]. Alternately, an initial guess for the phase velocity can be used to estimate the number of cycles for unwrapping. Figure 3 illustrates the spatial phase unwrapping. Using only the causal part of the NCF results in $-\pi/4$ phase shift relative to a great circle path prediction [*Harmon et al.,* 2008, 2009], so we add $\pi/4$ to the phase prior to tomographic inversion. We further eliminate phase measurements that yield equivalent phase velocities that are outside the range of the average phase

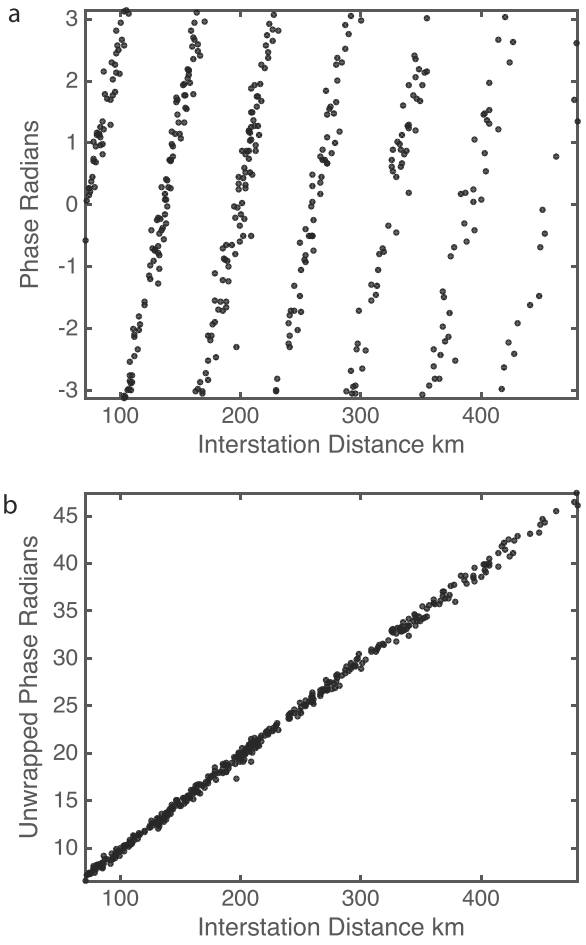

Figure 3. Example of spatial phase unwrapping. (a) Phase measured at 18 s period from NCF and (b) unwrapped phase at 18 s.

velocity ±0.2 km/s. The choice of ±0.2 km/s excludes 12 and 92 station to station phase measurements out of 392 at 18 and 33 s period, respectively, from the data set.

2.2. Data Processing of Teleseismic Events

Vertical component broadband seismic data from the ICEMELT and HOTSPOT arrays were used to measure the amplitude and phase of Rayleigh waves from 18 to 125 s period (Figures 2a and 2c). We selected events $M_S > 5.5$ with epicentral distances ranging from 20° to 150°, with focal depths < 200 km. We used a maximum of 209 events with good azimuthal distribution (Figure 2d).

Individual seismograms were processed as follows. We removed the instrument response. We then use frequency-time analysis [*Landisman et al.*, 1969; *Levshin and Ritzwoller*, 2001] with phase matched filtering [*Herrin and Goforth*, 1977] to isolate the Rayleigh wave fundamental mode. We then measure the amplitude and phase of the Fourier transformed phase matched filtered seismogram at each frequency of interest. We required a minimum signal-to-noise ratio (SNR) of 10 for a single station measurement, and we required a minimum of eight stations for an event to be included in the data set. We define SNR as the amplitude of the Rayleigh wave over the RMS amplitude for a 100 s segment of noise prior to the Rayleigh wave. Further requirements included a coherent signal across the array for the station/event group to be included in the inversion, which was determined from beamforming and described in section 2.3.

2.3. The 1-D Phase Velocity Inversion

We estimated the average phase velocity in the region using both the ambient noise and teleseismic data individually. For ambient noise at each frequency of interest, 6–50 s period, we find the best fitting zero order Bessel function of the first kind (J_0) of the form $A^*J_0(\omega s/c)$ to the real Fourier component (symmetric component of NCF) of all useable station-to-station NCF, where A is the amplitude, ω is angular frequency, s is station to station separation, and c is phase velocity. We solve for A and c by searching over phase velocity from 3.0 to 5.0 km/s in 0.01 km/s intervals and solving for the least squares amplitude, A, at each interval. The best fit is determined by the minimum variance of the data residual, i.e., real Fourier components minus the predicted best fit Bessel function. All frequencies of interest in this study produced a single minimum. While the amplitude may not be well recovered, due to scatter in the data caused by source distribution, the phase velocity is well recovered, because the best fit is determined by matching the zero crossings of the Bessel function. We used this approach to demonstrate its utility, because we do not require any prior information about the velocity structure to estimate the phase.

For the teleseismic data, we use a beamforming technique to determine the average phase velocity across the array and to identify events that are not coherent across the array. For each event, we assume a single

plane wave model and generate a beamformer output as a function of frequency, phase velocity, and back azimuth with respect to the source $b(\omega,\theta,c) = p^{\mathsf{T}}\mathbf{C}(\boldsymbol{\omega})p$, where $p = \exp(-i\mathbf{k}\cdot\mathbf{x})$, a vector of plane wave predictions at station location x for a wave number k which is equal to $\omega/c^{*}\mathbf{e}$, where $\mathbf{e}$ is the direction cosines as a function of back azimuth, and $\mathbf{C}$ is the cross-correlation matrix of the vector of complex dispersion measurements at each station at angular frequency ω. At each frequency of interest (0.008–0.056 Hz or 18–125 s period) we search over θ from $-40°$ to 40° in 1° increments of the back azimuth, and over phase velocity, c from 3.2 km/s to 4.5 km/s in 0.01 km/s increments to find the greatest beamformer output for a given event. If the normalized beamformer output (normalized so the maximum is 1.0) is < 0.60, the event is rejected as incoherent; otherwise, it is included in the average of all events. We chose 0.60 for beamformer output as it allows for complications in the wavefield that are later accounted for with a two-plane wave approximation. We found that the fit for the two-plane wave inversion for events below 0.60 was very poor. The average phase velocity is determined by a weighted mean of all acceptable events where the weights are equal to the normalized beamformer output.

The 1-D dispersion model is used as the starting model for the 2-D phase velocity inversions at each period.

2.4. The 2-D Phase Velocity Inversion

We adapt the two-plane wave tomography (TPWT) method [*Forsyth and Li*, 2005; *Yang and Forsyth*, 2006] to include ambient noise phase measurements in the inversion, which we refer to hereafter at the Joint ANT/TPWT inversion. The TPWT method approximates the incoming wavefield as the superposition of two plane waves and uses 2-D sensitivity kernels [*Zhou et al.,* 2004] to account for the effects of scattering. Equation (1) gives the forward model for the predicted complex Fourier component each event-station pair at a given angular frequency:

$$\begin{aligned} F(x_j,x_i,\omega) = {} & A_{1,j}\left(1+\delta\ln\left(A_{1,j}\right)\right)\exp\left(-i\left[\omega\cos\left(\theta_{1,j}\right)\frac{s_i}{\bar{c}}+\varphi_{1,j}+\delta\psi_{1,j}\right]\right)+ \\ & A_{2,j}\left(1+\delta\ln\left(A_{2,j}\right)\right)\exp\left(-i\left[\omega\cos\left(\theta_{2,j}\right)\frac{s_i}{\bar{c}}+\varphi_{2,j}+\delta\psi_{2,j}\right]\right) \end{aligned} \tag{1}$$

where F is the predicted complex vertical Fourier component for the event located at x_j, and station located at x_i and angular frequency ω. $A_{1,j}$ and $A_{2,j}$ are the plane wave amplitudes for each respective plane wave for event j. $\delta A_{1,j}$ and $\delta A_{2,j}$ are the amplitude variation caused by velocity heterogeneity. s_i is the distance from the station to a local reference point in the great circle path to the event, $\bar{c}$ is the average phase velocity determined in section 2.3, $\theta_{1,j}$ and $\theta_{2,j}$ are the azimuths of the plane waves for the event, $\varphi_{1,j}\,\varphi_{2,j}$ are the initial phase of the plane waves and $\delta\psi_{1,j}\,\delta\psi_{2,j}$ are the phase delays caused by velocity heterogeneity.

The changes in amplitude and phase δA and $\delta\psi$ are determined from analytic 2-D sensitivity kernels [*Y Zhou et al.,* 2004]:

$$\delta\ln(A) = \iint K_A\frac{\delta c}{\bar{c}}\,\mathrm{d}x\mathrm{d}y \tag{2}$$

$$\delta\psi = \iint K_\psi\frac{\delta c}{\bar{c}}\,\mathrm{d}x\mathrm{d}y \tag{3}$$

where phase velocity perturbation, $\delta c = c - \bar{c}$ and K indicates the sensitivity kernel for either amplitude (subscript A) or phase (subscript ψ).

For the ambient noise data, we invert only the phase, and we assume the following forward model:

$$F(x_i,x_j\omega) = \omega\frac{s_{i,j}}{\bar{c}}+\delta\psi_{i,j} \tag{4}$$

where i and j subscripts indicate stations located at x_i and x_j, $s_{i,j}$ is the interstation distance, and $\delta\psi_{i,j}$ is defined by equation (3). Previous theoretical work indicates that for a uniform noise source distribution, these types of sensitivity kernels are valid [*Nishida*, 2011; *Tromp et al.,* 2010]. The data processing for the noise is performed so that the effective source distribution is homogenized as much as possible, and as pointed out by *Harmon et al.* [2010], the phase error for interstation spacing greater than twice the seismic wavelength is typically less than 1% with typical source distributions in coastal areas.

We use a nodal parameterization for phase velocity structure (Figure 4), where the sensitivity kernels in equations (2) and (3) are averaged onto each node, and the integration is evaluated numerically over the nodes. The node spacing is 0.5° by 0.5° with an exterior set of nodes with 1.0° spacing, to absorb velocity

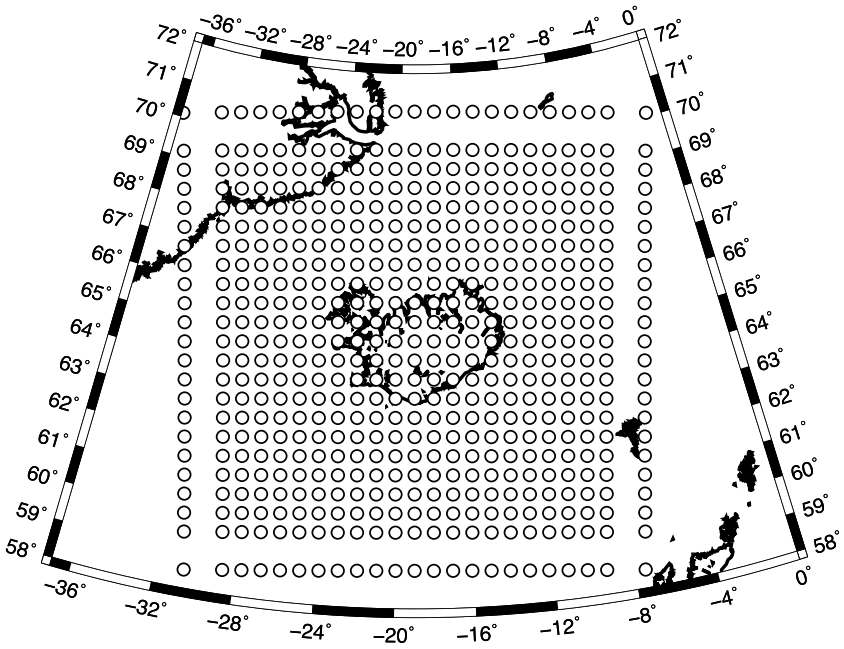

Figure 4. Nodal parameterization used in this study. White circles indicate node locations.

heterogeneity outside the array, which are also given a larger a priori covariance to allow for greater velocity variations. The sensitivity kernels for both the ambient noise and teleseismic data sets are averaged for each node using a Gaussian weighting assuming a width of 80 km. We use this Gaussian weighting scheme later to interpolate the velocity at the nodes onto a continuous grid.

We invert ambient noise and teleseismic data for phase velocity perturbation, δc, at each node, six plane wave parameters for each teleseismic event, $A_{1,j}$, $A_{2,j}$, $\theta_{1,j}$, $\theta_{2,j}$, $\varphi_{1,j}$,$\varphi_{2,j}$, and a station amplitude correction for the teleseismic data. We use an iterative-damped least squares inversion, in two stages using the following equation.

$$\delta m_{i+1} = \left(G^T C_{nn}^{-1} G + C_{mm}^{-1}\right)^{-1} \left(G^T C_{nn}^{-1} \delta d - C_{mm}^{-1}[m_i - m_0]\right) \quad (5)$$

where m_i is the model vector at iteration i, δm_i is the change to the model vector at iteration i, G is the matrix of partial derivatives with respect to the six incoming wavefield parameters and node phase velocities, C_{nn} is the data covariance matrix, assumed to have only diagonal elements, C_{mm} is the a priori model covariance matrix, where we have only diagonal terms, and δd, which is the data residual vector [*Tarantola and Valette*, 1982].

In the first stage, the teleseismic data are given an equal a priori standard deviation for C_{nn} of 0.4, and noise phase data are given a standard deviation of 0.2. The numbers are nondimensional because the teleseismic data are normalized by their RMS for each event and phase data are in radians. In the second stage, the a priori standard deviations for the data from each teleseismic event are reset to the event misfit standard deviation, and the noise data are scaled to their misfit standard deviation in the data covariance matrix. We find this combination (0.4 and 0.2 for standard deviation) works well and gives roughly equal weight to both data sets. For the a priori model covariance, we assume that the model standard deviation is 0.2 km/s for phase velocity. Errors for the phase velocities presented here are formal errors from the linearized least squares inversion, based on the a priori data covariance indicated above.

In this paper, we present results for the 2-D phase velocity maps for 18–50 s period using the Joint ANT/TPWT inversion and the TPWT inversion and the ANT inversion individually. We performed TPWT tomography for the longer periods, 67–125 s, to permit shear velocity inversions. However, the anomaly structure we recovered is similar to what was found in a previous study [*Li and Detrick,* 2004, 2006], so we do not present them here.

2.5. Shear Velocity Inversion

We illustrate the effect of the Joint ANT/TPWT inversion on the dispersion curves from different parts of our phase velocity maps and the subsequent shear velocity inversions. We use the same damped iterative least

squares inversion scheme presented in equation (5), where **m** is the shear velocity model and **d** is our phase velocity dispersion curve from 18 to 125 s period. The matrix of partial derivatives relating changes in shear velocity to changes to phase velocity, *G*, is calculated using DISPER80 [*Saito*, 1988]. We also solve for crustal thickness using a partial derivative calculated using a finite difference approximation. C_{nn} is the data covariance matrix, which we assume consists of diagonal entries with the corresponding variances of the phase velocities at each period. C_{mm} is the model covariance matrix, and we impose a smooth second derivative structure onto the shear velocity model, with a scaling of $(0.1\ \mathrm{km/s})^2$; we assume an a priori error for crustal thickness of 50 km essentially leaving the parameter undamped. We assume a *Vp*/*Vs* ratio of 1.8. We parameterize the model as a stack of layers, with thickness of 10 km in the shallowest layer, increasing to 25 km thick through the upper 400 km of the mantle, with a total of 18 layers. Crustal thickness changes are accommodated in the second layer.

3. Results

3.1. Resolution Tests Checkerboards

Raypaths for 18, 25, and 33 s period are shown in Figure 5 and 40, 45, and 50 s period in Figure 6 and illustrate how the number of raypaths increase with increasing period for the teleseismic data set, while the number of raypaths decreases for the ambient noise data set. Specifically, for the teleseismic inversions for 18, 25, 33, 40, 45, and 50 s period, there are 464, 1273, 2462, 2340, 2630, and 2795 station-earthquake pairs and 312, 225 144, 89, 63, and 36 station-to-station paths for ambient noise, respectively. Resolution outside the array comes from the crossing raypaths outside the array in the teleseismic inversion [*Forsyth and Li*, 2005].

A checkerboard test illustrates the utility of the joint inversion at 18 s (Figure 7) where the teleseismic data set is smallest and where we expect the greatest enhancement in resolution for the Joint ANT/TPWT inversion. The input for our checkerboard test is shown in Figure 6d, with a ±2.5% velocity anomaly for the average phase velocity, with an anomaly dimension of $1° \times 1°$. We use equation (1) to calculate the synthetic data for the earthquake-station pairs used in the teleseismic data set and equation (4) to generate the synthetic data for the ambient noise station-to-station pair data set. At < 30 s period, the incoming wavefield often deviates significantly from a single plane wave, often requiring a significant contribution from a second plane wave in the TPWT inversion [*Forsyth and Li*, 2005]. So for our checkerboard test we use a complicated incoming wavefield with two plane waves of equal strength and $-10°$ and 10°, respectively, off the great circle path, with zero initial phase for both plane waves. Although we have not modeled the entire source to receiver wave propagation here, previous work has shown that the two-plane wave method and its parameterization is effective at preventing heterogeneity outside the study region from being mapped into the area of interest [*Yang and Forsyth*, 2006]. For completeness, we present similar checkerboard tests for $1° \times 1°$ anomalies for 20–50 s period, using a single plane wave with 0.0 initial phase along the great circle path in Figure S1 in the supporting information.

Using only the teleseismic data, the input structure is well recovered on the western half of mainland Iceland, with smearing evident in the east and northeast (Figure 7). Outside the array and offshore Iceland, smearing is visible at all azimuths in most fast and slow anomalies where there are fewer crossing raypaths. The anomaly magnitude is within 2% of the true value in the best resolved single anomaly in the center of Iceland, although the anomaly structure is muted. The teleseismic inversion alone does not recover the wavefield parameters well and suggests that there is a strong trade-off at this frequency with the wavefield parameters and the velocity structure. The ambient noise recovers the structure well within the array, with smearing at the edges of the array caused by decreased resolution at the edges of the finite frequency kernels. The method recovers the amplitude of the anomalies within 1% across this region, slightly under predicting the magnitude of the anomalies. There is some resolution outside of the array due to the finite-frequency kernels used but does not recover the fast anomalies directly north and south of the center of Iceland. The Joint ANT/TPWT inversion recovers the pattern within the array just as well as the ANT inversion. The Joint ANT/TPWT inversion recovers the anomaly pattern better than the individual ANT and TPWT inversions outside the array. The Joint ANT/TPWT inversion does particularly well where there are crossing raypaths in the teleseismic data. Notably, the smearing in the northeast of the study region is much less pronounced in the joint inversion than in the teleseismic. As we observed in the ANT test, the amplitude difference between the true and recovered anomalies is less than 1%, but again, the magnitude of the anomalies is muted. The wavefield parameters are well recovered within error for 41 out of 46 events.

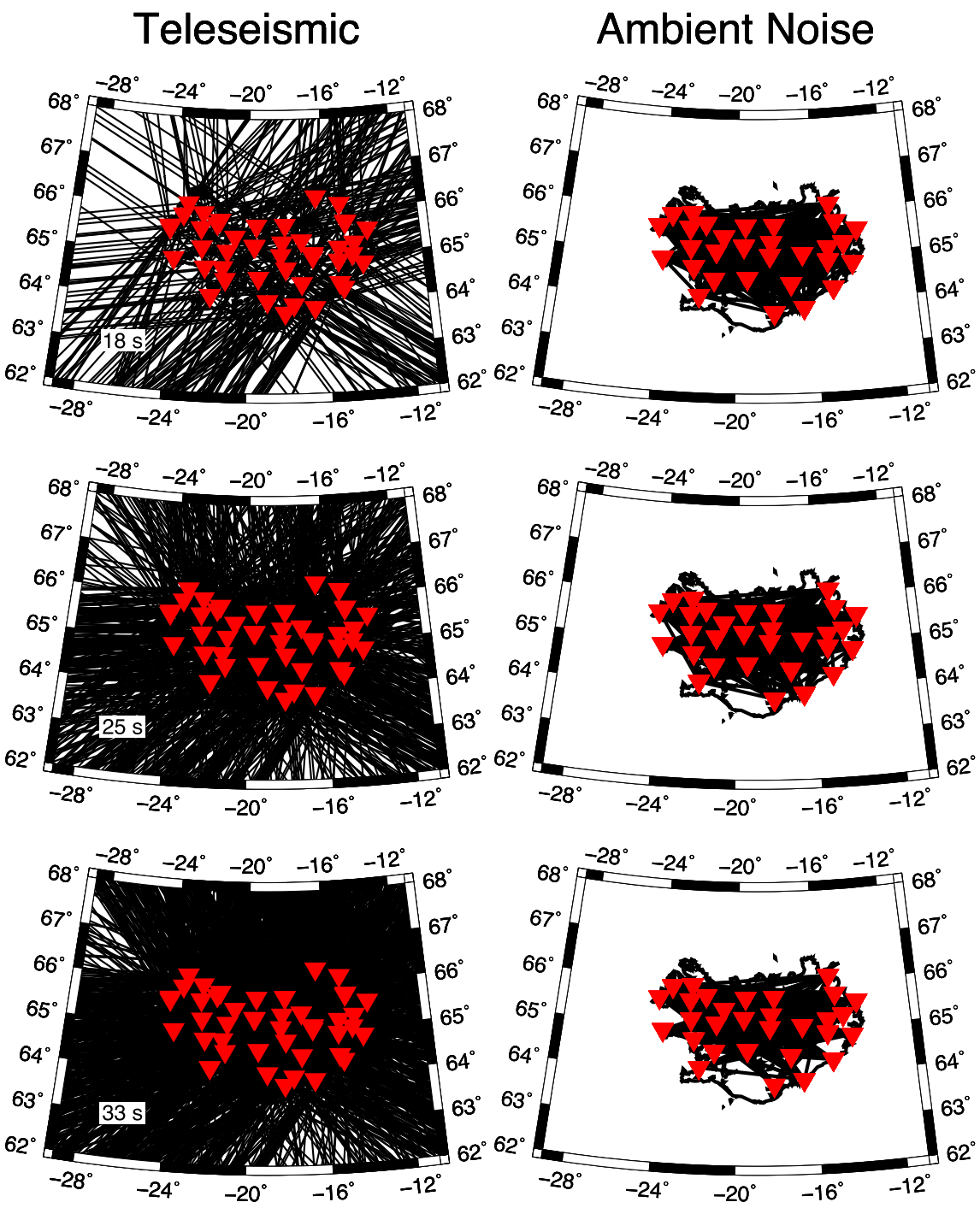

Figure 5. Raypaths for (top row) 18 s, (middle row) 25 s, and (bottom row) 33 s period for (left column) teleseismic and (right column) ambient noise. For the teleseismic there are 464, 1273, and 2462 station-earthquake pairs for the teleseismic data and 312, 225, and 144 station-to-station paths for ambient noise for 18, 25, and 33 s, respectively.

We performed similar checkerboard tests for 20–50 s period with the complicated incoming wavefield. As the period increased the checkerboard recovery for the ANT becomes worse with strong lateral smearing in an E-W direction (Figure S1). In turn, the checkerboard recovery becomes worse for both the Joint ANT/TPWT and TPWT with increasing period, as there was a very strong trade-off between the wavefield parameters and the velocity structure.

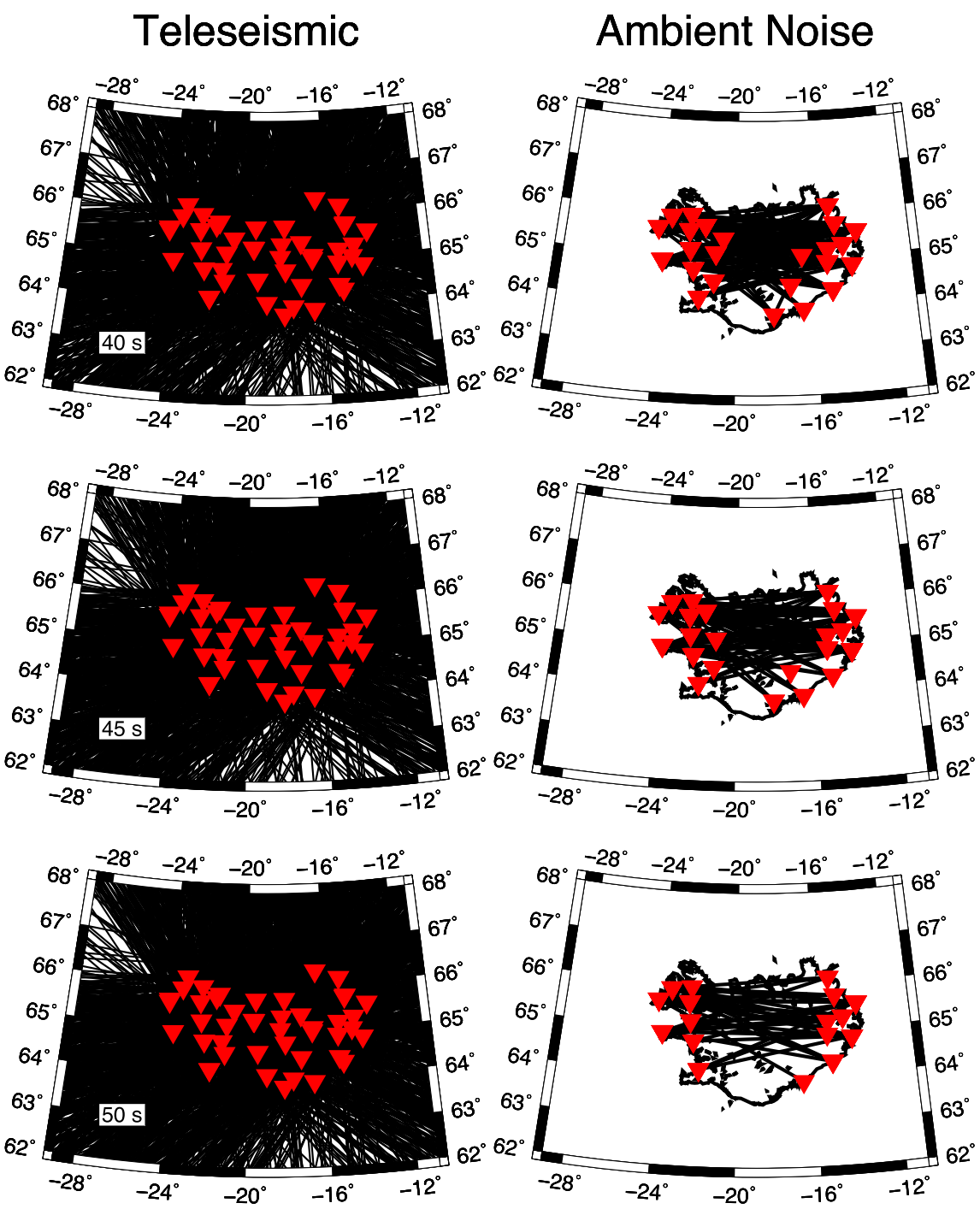

Figure 6. Raypaths for (top row) 40 s, (middle row) 45 s, and (bottom row) 50 s period for (left column) teleseismic and (right column) ambient noise. For the teleseismic there are 2340, 2630, and 2795 station-earthquake pairs for the teleseismic data and 89, 63, and 36 station-to-station paths for ambient noise for 40, 45, and 50 s, respectively.

3.2. The 1-D Phase Velocity Structure and Average 1-D Shear Velocity Structure

The 1-D dispersion curves measured from ambient noise and teleseismic data are presented in Figure 8a. The velocities range from 3.12 ± 0.01 km/s at 6 s to 4.23 ± 0.03 km/s at 167 s. Where the ambient noise and teleseismic phase velocity estimates overlap, they are within their respective formal 2 times standard error bars. In general, the error for the ambient noise is smaller, but the two methods yield similar results.

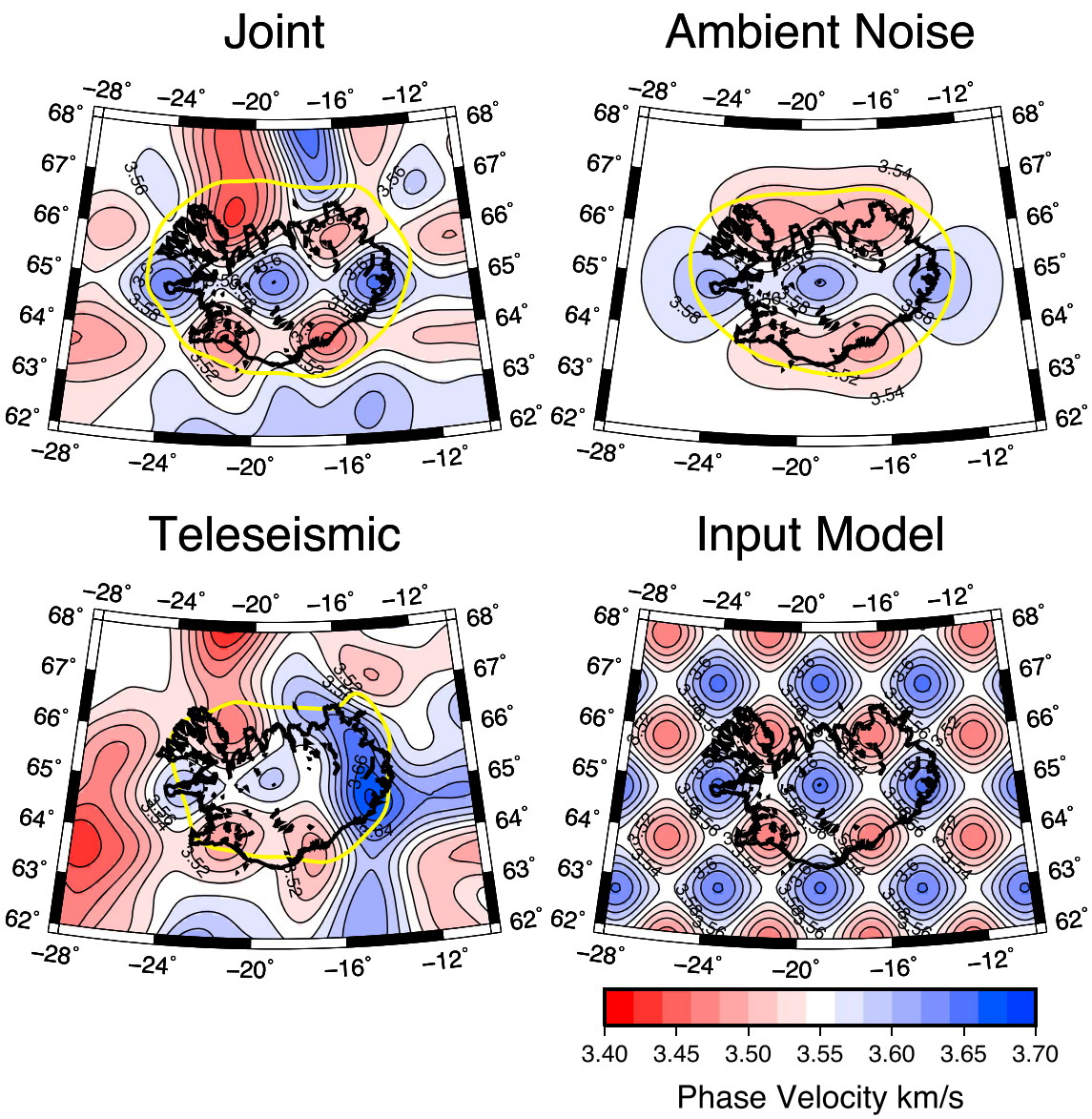

Figure 7. Comparison of checkerboard tests for 18 s period for teleseismic, ambient noise, and the joint inversion. Yellow lines indicate 0.06 km/s error contour for the joint inversion and teleseismic inversions and 0.10 km/s error contour for the ambient noise.

The shear velocity structure from our inversion is presented in Figure 8b. We observe crustal velocities (3.22–3.77 km/s) in the upper 30 km. The uppermost mantle consists of a fast lid, with a maximum velocity of 4.05 ± 0.03 km/s, centered at ~43 km depth. There is a low-velocity zone beneath, with a velocity minimum of 3.92 ± 0.03 km/s at 117 km depth. In Figure 8c we show the depth sensitivity kernels for the shear velocity inversion for 6, 18, 25, 33, 45, and 100 s period, which indicate the depths of peak sensitivity at each period.

3.3. The 2-D Phase Velocity Structure

The 2-D phase velocity maps from ANT, TPWT, and Joint ANT/TPWT tomography are compared in Figure 9 for 18, 25, and 33 s, in Figure 10 for 40, 45, and 50 s period with standard error presented in Figures 11 and 12.

At 18 s period, the Joint ANT/TPWT, TPWT, and ANT recover similar structures within Iceland (Figure 9). There is a broad, low-velocity region centered beneath the intersection of the Northern, Western, and Eastern Volcanic Zones. The Joint ANT/TPWT inversion has a minimum value of 3.42 ± 0.02 km/s, while the TPWT has a minimum of 3.50 ± 0.04 km/s, and the ANT has a minimum value of 3.41 ± 0.04 km/s in this region.

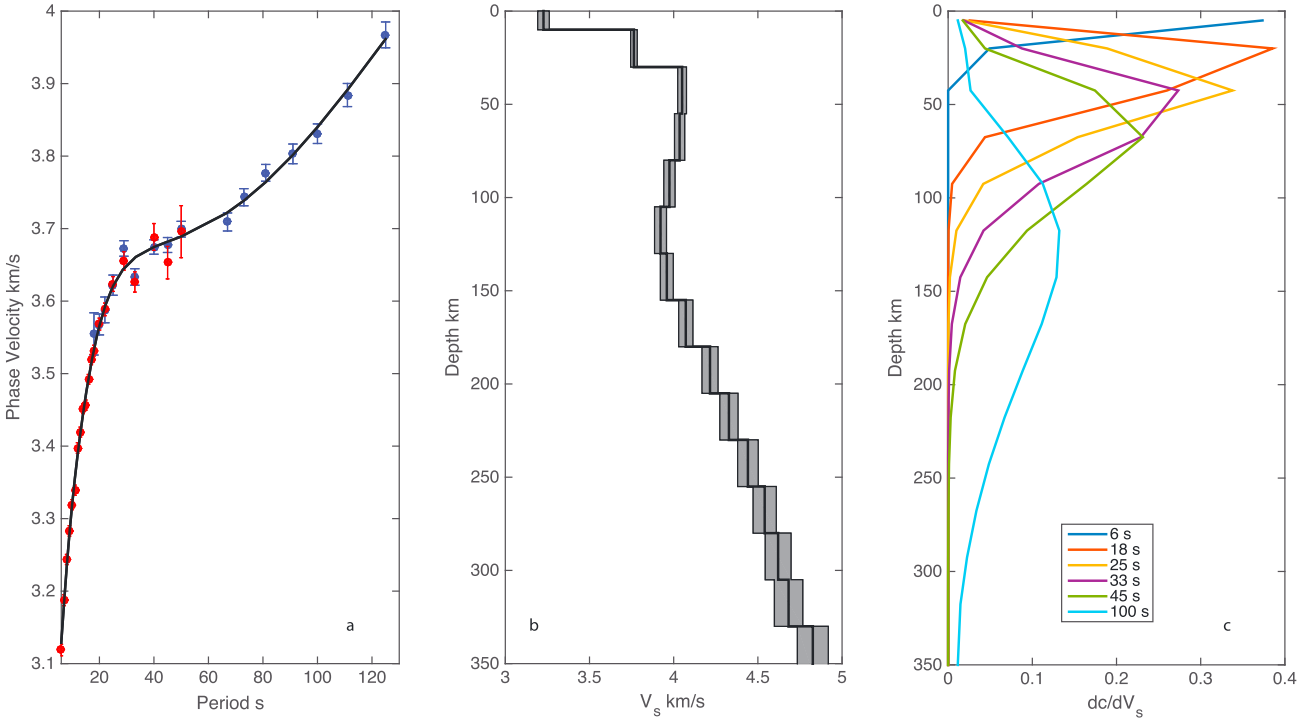

Figure 8. (a) Phase velocity comparison between teleseismic (blue) and ambient noise (red) 1-D phase velocity estimates with 2σ errorbars and best fit shear velocity model dispersion (black line). (b) Best fit shear velocity model (black line) and formal error bounds (grey shaded region). (c) Sensitivity kernels for Rayleigh waves at select periods.

Beneath the Northwest Fjords, there is a high-velocity region, with TPWT producing a maximum of 3.65 ± 0.05 km/s, ANT with a maximum of 3.68 ± 0.06 km/s, and the Joint ANT/TPWT inversion producing a maximum of 3.73 ± 0.04. The agreement between the methods for the maxima is within error, although the maximum for the TPWT is located farther west than in the ANT and Joint ANT/TPWT inversions. In the TPWT, which has resolution offshore, there is an indication of a low-velocity region offshore of the Reykjanes peninsula and offshore of the Northern Volcanic Zone (NVZ), which persists in the Joint ANT/TWPT inversion. At 25 s period, the phase velocity maps show similar structures to the 18 s period maps, with a low velocity centered beneath the intersection of the volcanic rift zones and high-velocity regions beneath the Northwest Fjords and to the south of the island. The high-velocity region to the south has lower values in the TPWT than in the joint inversion by ~0.02 km/s, but the values are within error.

The velocity structure changes to a low-velocity region that underlies the Northern, Eastern, and Western Volcanic Zones in the 33–50 s phase velocity maps for the joint, TPWT, and ANT. In the 33 s phase velocity maps all three methods have similar minimum values around ~3.58 km/s in the region. High velocities up to 3.79 ± 0.03 from the joint inversion (3.72 ± 0.04 km/s TPWT and 3.80 ± 0.09 km/s ANT) are observed beneath the Northwestern Fjords. Offshore, low velocities are observed near the Reykjanes peninsula (3.52 ± 0.04 km/s minimum in the Joint ANT/TPWT inversion), with higher velocities the surrounding the island otherwise up to ~3.72 km/s in the TWPT and Joint ANT/TPWT inversion. The high velocities surrounding Iceland are more continuous in the Joint ANT/TPWT than in the TPWT.

At the 40–50 s periods, as the number of ambient noise data decrease, the differences between the TPWT and Joint ANT/TPWT are minimized as the inversions are weighted more heavily toward the teleseismic data. However, differences in the anomaly pattern around the NW Fjords can be observed, specifically the high-velocity anomaly tends to become more centered beneath the NW Fjord Peninsula in the Joint ANT/TPWT relative to the TPWT. The ANT indicates a broad low-velocity region across the center of Iceland but appears to be heavily smeared, as might be expected given the mostly E-W paths across Iceland.

We quantify the difference between the phase velocity maps produced by the different methods and propagate the formal errors of the inversion to assess where differences between the phase velocity maps are

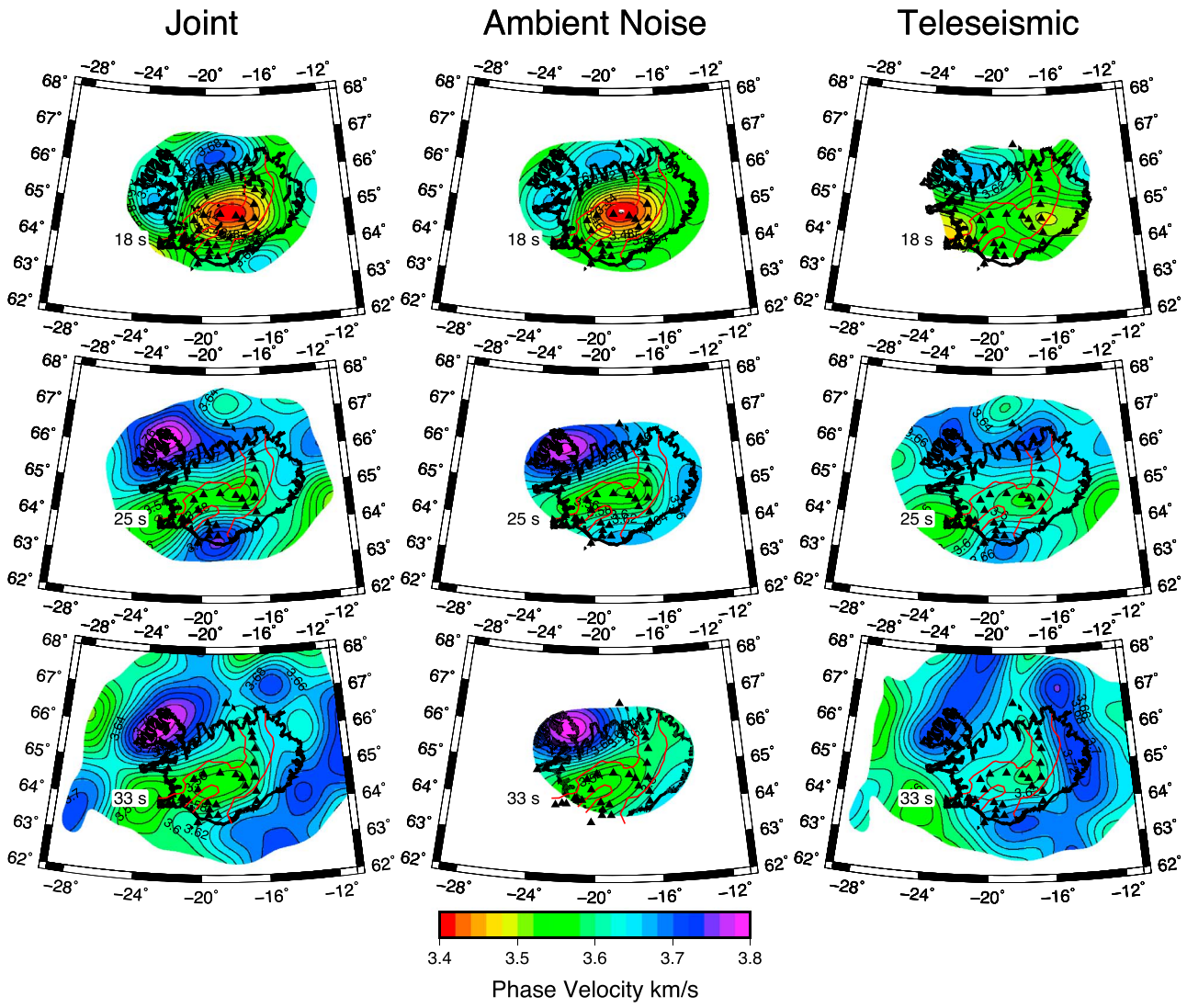

Figure 9. Phase velocity maps. Comparison of (third column) teleseismic, (second column) ambient noise, and (first column) Joint ANT/TWPT phase velocity tomography for (top row) 18 s, (middle row) 25 s, and (bottom row) 33 s period. The ANT is masked using the 0.1 km/s error contour, while the Joint ANT/TPWT and TPWT are masked with the 0.06 km/s error contour. Black triangles show the location of the Holocene volcanism, and red lines indicate the lateral extent of Quaternary volcanism in the Volcanic Zones.

significant from zero at the 2σ error level (Figure 13). We present the difference between the Joint ANT/TPWT and TPWT tomography for 18, 25, 33, 40, and 45 s period and the difference between the Joint ANT/TPWT and the mean of the ANT and TPWT maps (mean phase velocity map) for 18, 25, and 33 s period. We note that alternative weighted averages could be used for the mean approach. In our case the error is lower and the number of observations greater for the TPWT, so standard weighting schemes would tend to weight the average toward the TPWT phase velocity map. We masked out (in white) the regions within the 0.06 or 0.05 km/s error contour the Joint ANT/TPWT and TPWT difference and the 0.10 km/s error contour for the Joint ANT/TPWT-mean phase velocity map and also greyed the region where the differences are not significant at the 2σ levels from the formal error propagation indicated in Figures 11 and 12 for the Joint ANT/TPWT errors. We do not present the difference between the Joint ANT/TPWT and the ANT because there were no significant differences between the models due to the larger formal errors in the ANT. For the same reason we do not present the difference maps for 40–50 s period between the Joint ANT/TPWT and mean phase velocity maps.

At 18 s period there are significant differences in phase velocity between the Joint ANT/TPWT and the TPWT tomography across the region by up to 0.15 km/s near the Western Volcanic Zone. There are other significant

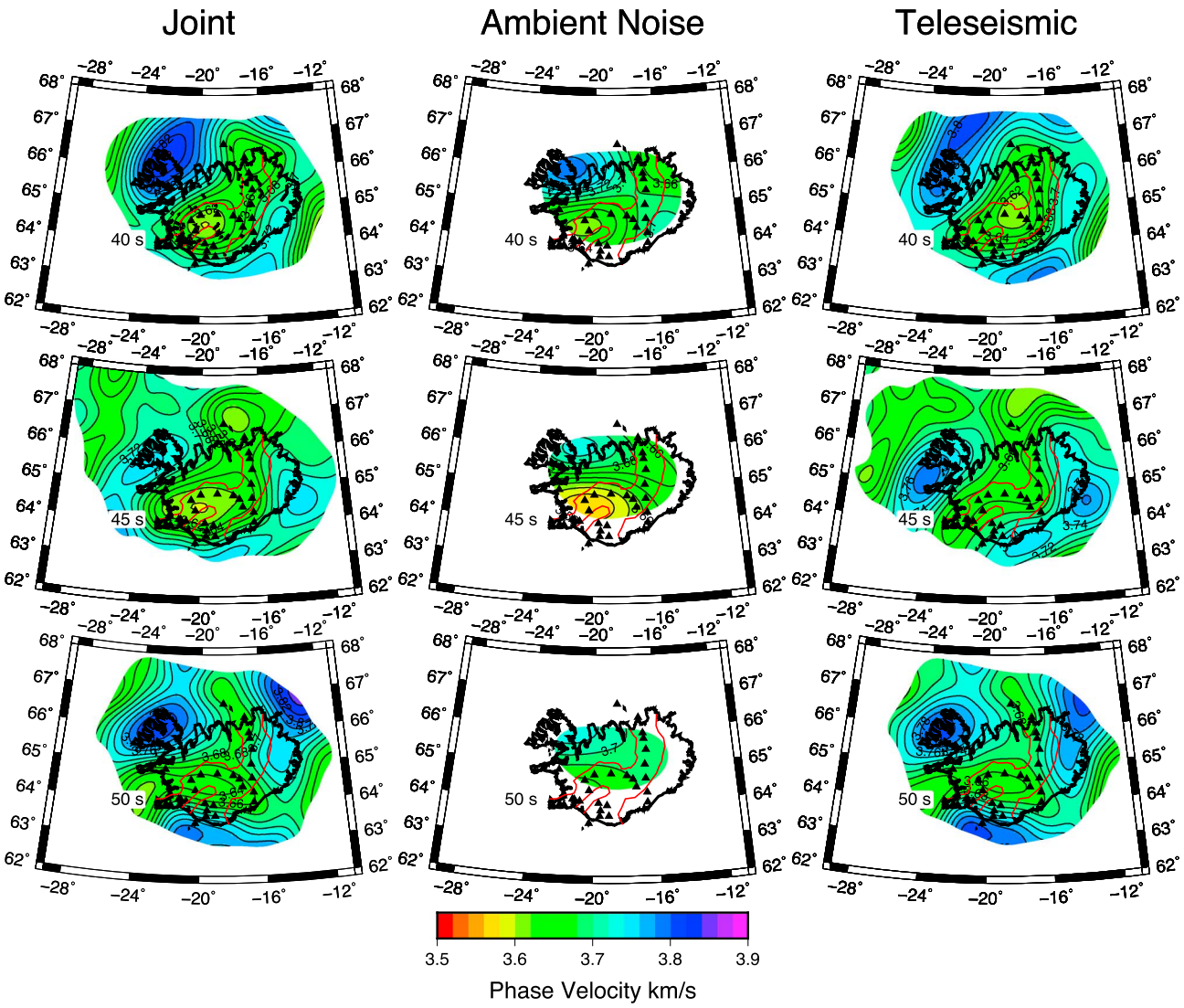

Figure 10. Phase velocity maps. Comparison of (third column) teleseismic, (second column) ambient noise, and (first column) Joint ANT/TPWT tomography for (top row) 40 s, (middle row) 45 s, and (bottom row) 50 s period. The ANT is masked using the 0.1 km/s error contour, while the Joint ANT/TPWT and TPWT are masked with the 0.05 km/s error contour. Black triangles show the location of the Holocene volcanism, and red lines indicate the lateral extent of Quaternary volcanism in the Volcanic Zones.

differences required offshore to the north, southwest, and east. There is a maximum difference of 0.08 km/s between the Joint ANT/TPWT and the mean phase velocity maps, with a similar pattern to the Joint-Teleseismic difference map.

At 25 and 33 s period, the significant changes to the models between the Joint ANT/TPWT and the TPWT are located at the coastlines. The biggest differences between the models occur near the NW Fjords, which have maximum differences of 0.12 km/s and 0.11 km/s at 25 and 33 s period, respectively. At 25 and 33 s period, there are also large differences near the northern extent of the Northern Volcanic Zone/Tjornes Fracture Zone with maximum differences of 0.08 km/s, and at 33 s there is also a significant difference of 0.08 km/s near the Reykjanes Peninsula. In the difference maps for the Joint ANT/TPWT and the mean phase velocity map there are a few small areas near the NW Fjords for both 25 and 33 s period, and a smaller region near the southern extent of the Southern Volcanic Zone at 25 s period.

At 40 and 45 s period, significant differences between the Joint ANT/TPWT and TPWT are present within the Volcanic Zones, with values of 0.04 km/s and 0.06 km/s, respectively. At 40 s there is also a significant change required near the NW Peninsula with a maximum of 0.06 km/s.

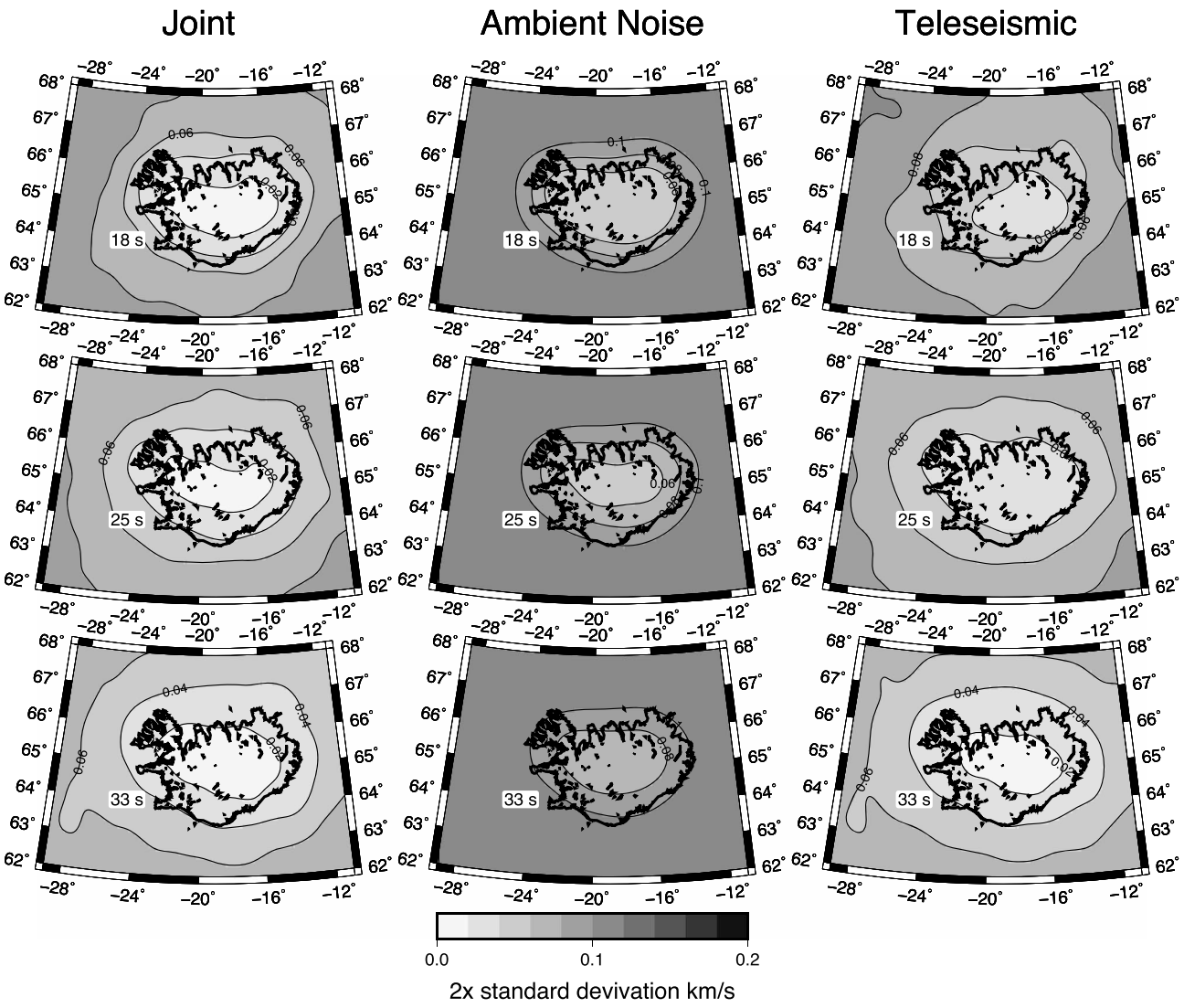

Figure 11. Standard error for phase velocity maps. Comparison of (third column) TPWT, (second column) ANT, and (first column) Joint ANT/TPWT phase velocity error from tomography for (top row) 18 s, (middle row) 25 s, and (bottom row) 33 s period.

We assess the misfit in the inversions using the phase misfit, which is the difference between the predicted phase arrival time and the observed phase arrival time for ANT and TPWT and the Joint ANT/TPWT inversion. At all periods, the fits to the data are similar between the Joint ANT/TPWT, TPWT, and ANT. The residuals were visually normally distributed in all cases, and we report the mean and 2σ values for the phase misfit in Table 1. For example, the residual phase times for the Joint ANT/TPWT inversion at 18 s are 0.055 ± 2.254 s for the teleseismic data and 0.007 ± 1.343 s for the ambient noise data. For comparison, at 18 s the TPWT alone has a residual of 0.044 ± 1.939 s, while the ANT alone has a residual of -0.009 ± 1.383 s at 18 s. We note that there is some variation in the mean of the residuals, but their absolute values tend to be small $\ll 1$ s and likely are not significant. At 45 and 50 s period, the average misfit in the ambient noise data is larger at ~0.4 s in the Joint ANT/TPWT, but the standard deviation of the residuals has a similar value to the ANT inversions alone. In other words, the fit to the data is essentially the same in all cases; however, the joint inversion satisfies both data sets simultaneously.

3.4. Comparison of Shear Velocity Inversions Near the Volcanic Zones and on the NW Fjords

We compare dispersion curves and their best fit shear velocity models for two separate regions in Iceland, near the intersection of the Volcanic Zones and the NW Fjords (Figure 14). We choose these two regions to

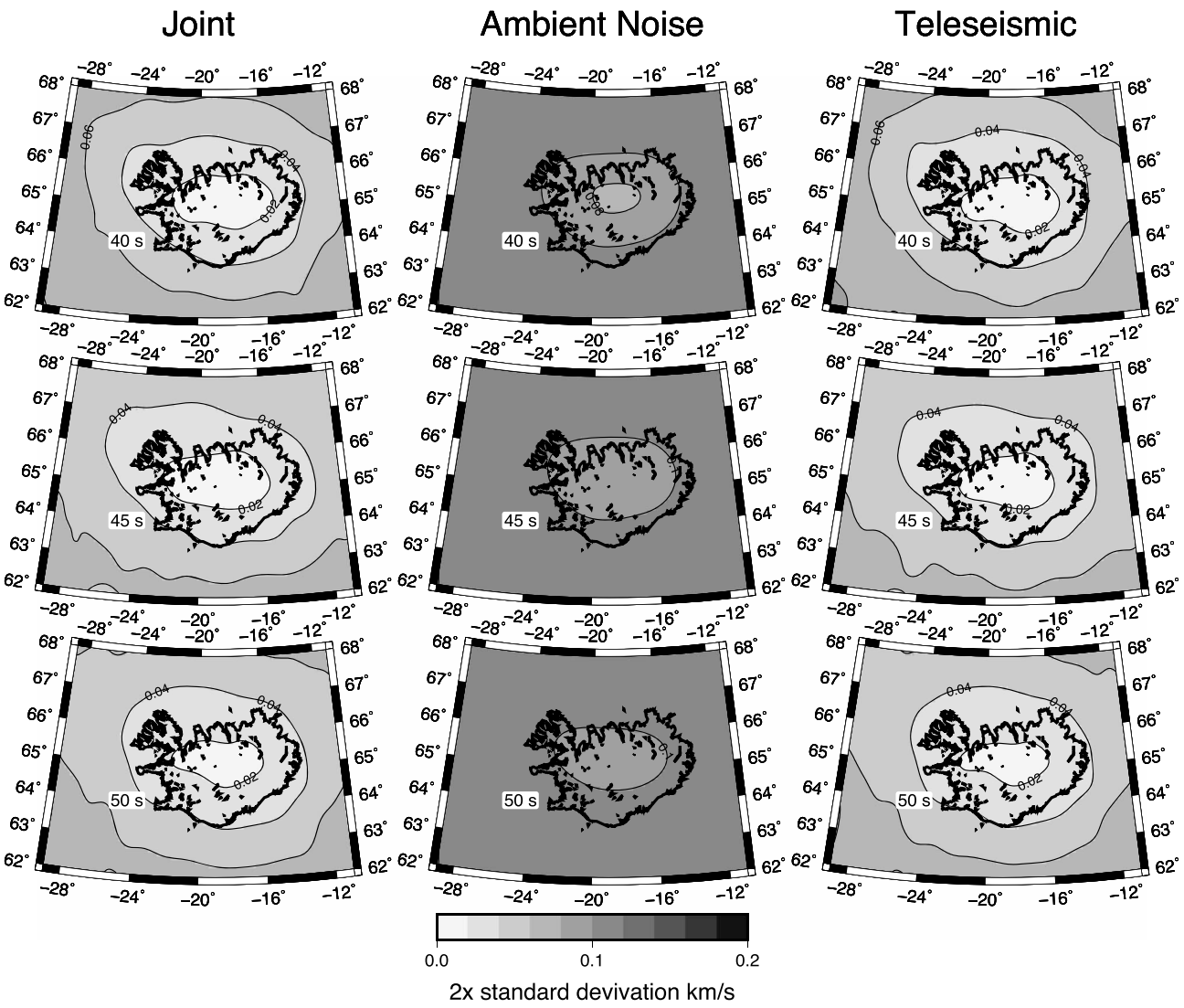

Figure 12. Standard error for phase velocity maps. Comparison of (third column) TPWT, (second column) ANT and (first column) Joint ANT/TPWT phase velocity error from tomography for (top row) 40 s, (middle row) 45 s, and (bottom row) 50 s period.

highlight the enhancements in the phase velocity maps produced by the Joint ANT/TPWT relative to the TPWT and the resulting shear velocity models. The region surrounding the Volcanic Zones is generally well resolved in both the JOINT ANT/TPWT and TPWT methods at most periods, while the NW Fjords is the location of significant differences between the models.

The Volcanic Zone example is located at 18.2°W, 64.7°N, labeled A in Figure 1. The dispersion curve for this point is fairly smooth for the TPWT (Figure 14a) and similarly for the Joint ANT/TPWT. The velocities are lower than the 1-D average for periods $<$ 80 s. The Joint ANT/TPWT and TPWT dispersion curves are within error of each other, except for 18, 25, and 29 s period. The Joint ANT/TPWT dispersion curve is visually smoother. The shear velocity results are similar for both the Joint ANT/TPWT and TPWT in this region, with overlapping error regions (Figure 14c), with low velocities ($<$=4.0 km/s) in the upper most mantle, with a weak or nonexistent fast lid. The crustal thickness in the Joint ANT/TPWT is 38 ± 10 km, while in the TPWT the crustal thickness is 33 ± 11 km.

The NW Fjord location is at 22.7°W, 65.7°N, labeled B in Figure 1. The dispersion curve for the TPWT for this location shows evidence for oscillations in the velocity across periods indicating this is a region where the model is less stable (Figure 14b). The dispersion curve for the Joint ANT/TPWT shows less strong oscillations

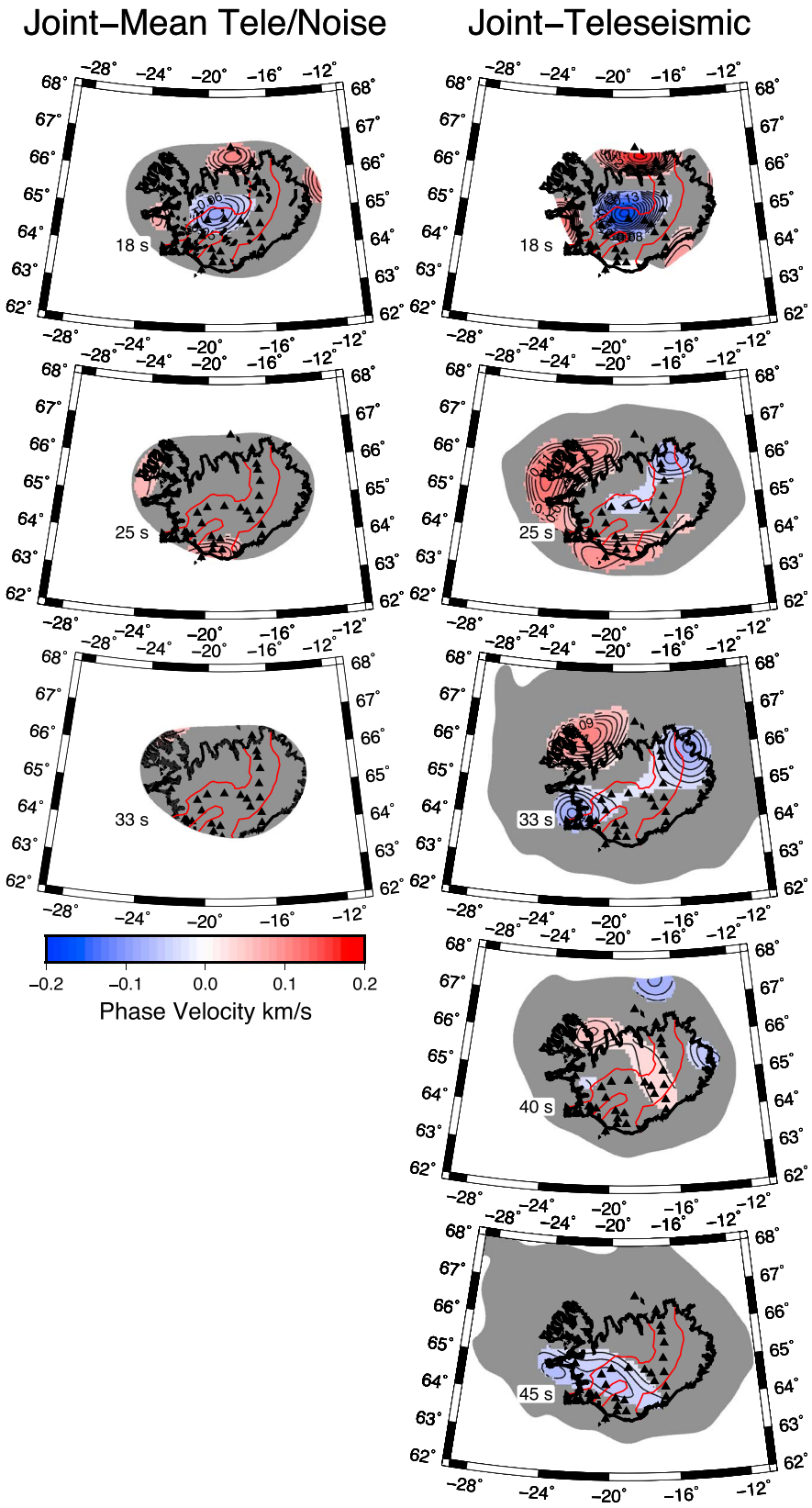

Figure 13. Comparison of phase velocity map differences between Joint ANT/TPWT and the mean of the TPWT and ANT phase maps (left column), and Joint ANT/TPWT and the TPWT phase maps (right column) for 18 s, 25 s, 33 s, 40 s, and 45 s period (from top to bottom).

Table 1. Phase Misfit in Seconds, Reported as the Mean Value, With 2 Times Standard Deviation of the Residuals[a]

	Joint ANT/TPWT		TPWT	ANT
Period (s)	Teleseismic Phase Misfit (s)	Ambient Noise Phase Misfit(s)	Teleseismic Phase Misfit (s)	Ambient Noise Phase Misfit(s)
18	0.055 ± 2.254	0.007 ± 1.343	0.044 ± 1.939	−0.009 ± 1.383
20	−0.045 ± 2.455	0.012 ± 1.611	−0.060 ± 2.082	−0.011 ± 1.618
22	0.011 ± 2.577	0.033 ± 1.798	0.047 ± 3.013	−0.001 ± 1.832
25	−0.016 ± 2.757	0.022 ± 2.250	−0.059 ± 2.652	−0.013 ± 2.261
29	0.065 ± 2.986	0.051 ± 2.589	0.031 ± 2.983	−0.025 ± 2.360
33	0.018 ± 3.273	0.060 ± 3.400	−0.012 ± 3.537	−0.023 ± 3.381
40	−0.012 ± 4.516	−0.033 ± 4.208	0.025 ± 3.856	0.049 ± 4.294
45	0.053 ± 3.704	0.436 ± 4.650	0.002 ± 3.784	0.029 ± 4.640
50	0.040 ± 4.386	0.350 ± 6.266	0.011 ± 3.842	−0.055 ± 6.484

[a]In all cases residuals were visually inspected to be normally distributed.

and again is visually smoother than the TPWT dispersion over the same frequency range. The shear velocity models are outside the formal error bars in the crust and uppermost mantle. The Joint ANT/TPWT has a slower crust that is 23 ± 5 km thick, as compared to the 29 ± 17 km thick crust for the TPWT. From 23 to 73 km depth the Joint ANT/TPWT is faster than the TPWT, with a maximum velocity of 4.43 ± 0.09 km/s, while the TPWT has a velocity of 4.07 ± 0.10 km/s in this depth range. The primary cause of this difference in the shear velocity is the least squares approach taken here is minimizing the oscillations in the dispersion at 18–50 s period and not fitting the dispersion well overall for the TPWT.

4. Discussion

4.1. Improvements Made Through Joint ANT/TPWT Inversion

For a complex incoming teleseismic wavefield, the Joint ANT/TPWT recovers the input checkboard anomaly better than the TPWT alone. Recovery of the anomaly pattern within the array is similar between the Joint ANT/TPWT and the ANT. The Joint ANT/TPWT recovers structure outside the array better than the ANT or TPWT inversions. The addition of the ambient noise data in the Joint ANT/TPWT helps resolve the incoming wavefield by constraining structure within the array and thus enhances recovery of structure outside the array. This improvement is particularly strong when the incoming wavefield is complex, and the ambient noise data can adequately constrain the structure inside the array, as in our testing.

The difference maps show that the Joint ANT/TPWT results in significant changes to the phase velocity maps relative to the TPWT and the mean of the TPWT and ANT (Figure 13). The biggest differences are observed at the shortest periods; however, relative to the TPWT significant changes can be observed up to 45 s period. Most of the change in the velocity models occurs at the edges of the well-resolved region, in agreement with the results from the checkerboard tests. The center of Iceland has minimal differences, as might be expected as these regions are well resolved by both data sets. The difference maps highlight that taking the mean of the independently derived phase velocity maps does not necessarily capture the trade-offs encapsulated in the Joint ANT/TPWT. Weighting the phase velocity maps by the amount of data in the mean of the TPWT/ANT phase velocity maps result would only increase the mismatch between the methods.

In the well-resolved Volcanic Zone the dispersion curve from both the Joint ANT/TPWT and TPWT are for the most part smooth and within error of each other, with only slight differences in the resulting shear velocity models. On the other hand, the NW Fjord dispersion curve from the TPWT is more oscillatory owing to increased trade-off with structure outside the array in the region. The addition of the ANT data in the Joint ANT/TPWT inversion results in a smoother dispersion curve, which results in a significantly improved shear velocity model. The Joint ANT/TPWT gives a fast lid structure, which is not present in the TPWT inversion. In practice, the oscillatory dispersion visible in the TPWT can be minimized, for instance, by modifying the starting model at adjacent periods to have similar structures. Alternatively, outliers could be culled from the dispersion curve on an ad hoc basis. The strength of the Joint ANT/TPWT approach is that these ad hoc procedures are not required.

The addition of ambient noise phase data to the teleseismic surface wave inversions builds on previous work [*Allen et al.,* 2002a; *Li and Detrick,* 2004, 2006] by extending the effective period range to 18 s period and by

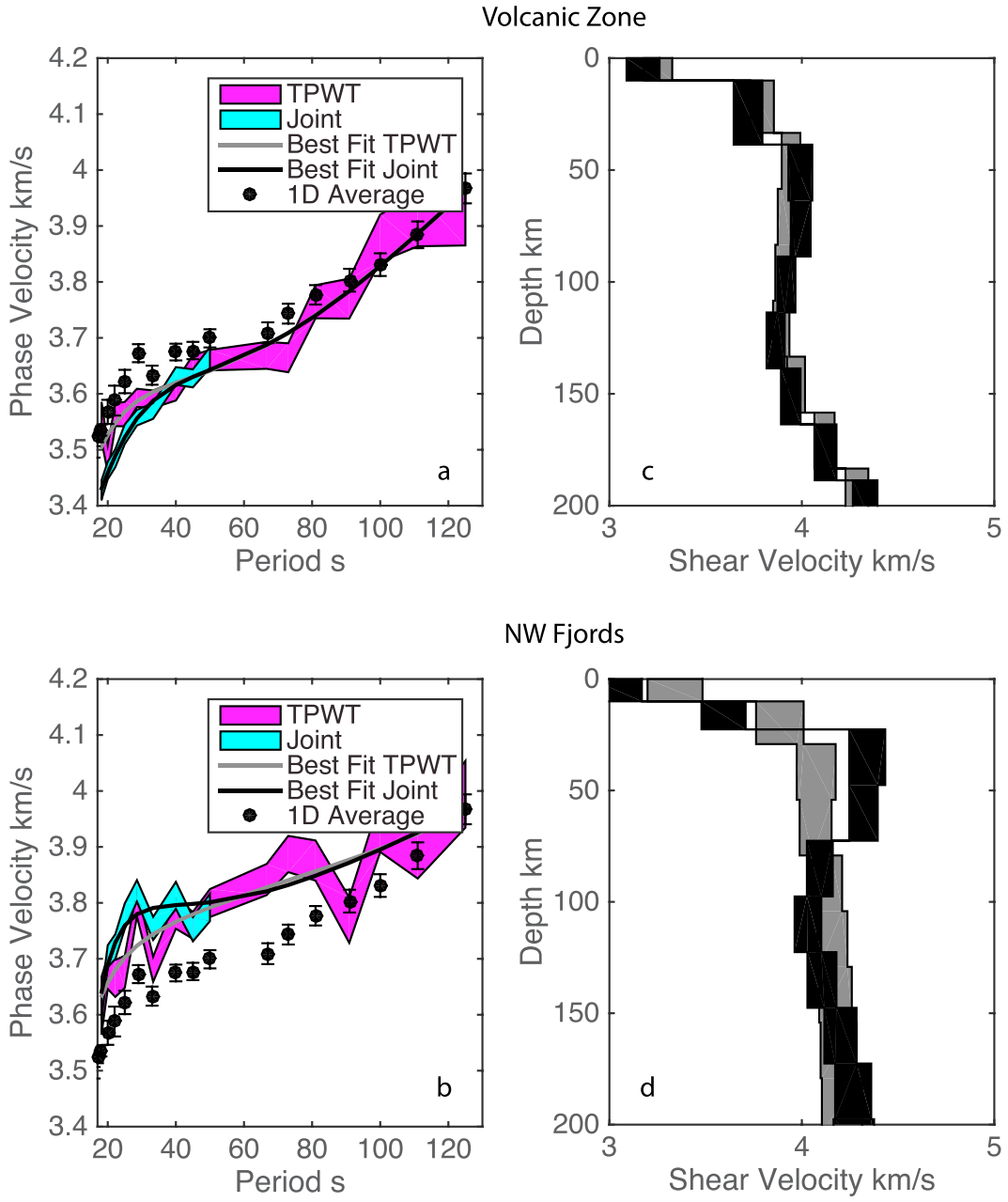

Figure 14. Comparison of (a and c) dispersion curves and corresponding (b and d) shear velocity model for point A (Volcanic Zone) and B (NW Fjord) in Figure 1. Dispersion curves and shear velocity models are shown as 2 times standard error regions.

improving the resolution outside the array at these shorter periods, particularly allowing us to image the structure offshore on the Reykjanes Ridge and Tjornes Fracture Zone and Kolbeinsey Ridge. In practice, the period range of the joint inversion could be extended to shorter periods than the 18 s used here, if the earthquake energy is present in the data and can be reliably measured, such as the case on the seafloor near the East Pacific Rise, where periods as short as 16 s were used [*Harmon et al.,* 2009, 2011]. This is most likely to be possible in regions with relatively simple structure such as ocean basins where short-period multipathing and scattering is less of a problem. In addition, longer-period surface waves can be recovered using ambient noise [*Schimmel et al.,* 2011; *Yang*, 2014], which could also be included in the joint inversion at longer periods than the 50 s period used here. The array aperture here was not sufficient for longer periods to be used.

4.2. Comparison to Previous Work

The low-velocity region in the center of Iceland observed in the 18 s–25 s period phase velocity maps is coincident with the crust of the overlapping portion of the Northern, Eastern, and Western Volcanic Zones and offshore with the location of the Reykjanes Ridge. Our result is consistent with previous surface wave studies in the region. Two studies that use the two-plane wave method and a Gaussian sensitivity kernel find a similarly broad low-velocity region with minimum values of ~3.48 at 22 s period [*Li and Detrick,* 2004, 2006]. Crustal thickness likely plays a role in generating the anomaly; however, the correlation between the lowest velocities and crustal thickness estimates from *P*-to-*S* and *S*-to-*P* receiver functions and active source studies and gravity anomalies is low [*Darbyshire et al.,* 2000; *Kumar et al.,* 2007]. Specifically, within the low-velocity region imaged here, the converted wave studies image regions of crustal thickness ranging from 26 km to 40 km [*Kumar et al.,* 2007], 30–40 km from active source and gravity analysis [*Darbyshire et al.,* 2000], and up to 45 km from an integrated study [*Allen et al.,* 2002b], with the thickest crust located beneath the transition from Eastern Volcanic Zone (EVZ) to the NVZ. The length scale of the change in crustal structure is similar to the length scales we were able to recover adequately in our checkerboard tests, so we do not believe that this feature is due to lateral smearing. The surface geology of Iceland is dominated by the basaltic eruptions that created the island, so it is likely the low velocities are associated with thermal anomalies and/or melt in the crust due to their connection with active volcanism and the location of the intersection of the Volcanic Zones.

At 33–50 s, the low-velocity region follows the trends of the Northern, Western, and Eastern Volcanic Zones and offshore the Reykjanes Peninsula onto the Reykjanes Ridge, with higher-velocity regions to the east and west. This likely represents the transition in sensitivity at these periods to a mantle fast lid/lithospheric structure as the peak sensitivity at these periods is ~ 40–50 km depth (Figure 8c). In addition, we observe lower velocities extending offshore toward the Tjornes Fracture Zone and the Kolbeinsey Ridge. The previous surface wave results for the region image a similar low-velocity region within the Volcanic Zones at 29 s period, with a minimum velocity of ~3.52 [*Li and Detrick,* 2004, 2006], although our result appears to follow the Volcanic Zones more closely, indicated by the red lines in Figures 9 and 10 and Quaternary volcanos in the black triangles. Some of the variation between our result and the previous studies using TPWT may be caused by different implementation of the methods such as the use of 2-D finite-frequency kernels in this study and different choices made during data selection.

The shear velocity models illustrate the transition in crustal thickness and fast lid thickness across the region. In the Volcanic Zone shear velocity model, the crust is thickened (38 ± 10 km), and a fast lid is not required. The crustal thickness is in the range of nearby single station estimates from receiver function results which range from 26 to 40 km [*Kumar et al.,* 2007] and an integrated study which finds a value of 40–45 km [*Allen et al.,* 2002b]. The mantle velocities are low ~4.00 km/s, which typically is interpreted in regions of active volcanism near spreading centers as being due to higher mantle temperature and/or the presence of partial melt [e.g., *Harmon et al.,* 2009, 2011]. Temperatures of 1600–1700°C are required to explain the slowest velocities assuming 1 cm grain size [*Jackson and Faul*, 2010]. Mantle potential temperature estimates from olivine thermometry indicate a temperature of 1616°C [*Putirka et al.,* 2007] and 1480–1520°C from rare Earth element modeling [*Maclennan et al.,* 2001]. Alternatively, a more moderate temperature, ~1500°C, and a small amount of partial melt (0.2%) could explain our result, assuming 1% melt yields 7.9% shear velocity decrease [*Hammond and Humphreys*, 2000]. In contrast, on the NW Fjord, which is ~15 million years old [*Martin et al.,* 2011] has a thinner crust (23 ± 5 km) and a fast lid from 23 to 73 km depth. Receiver functions image a crustal thickness of 26–38 km in this region [*Kumar et al.,* 2007] while another images a thickness of 25–30 km in the region [*Allen et al.,* 2002b]. The deeper mantle in the low-velocity zone is again quite slow ~4.00 km/s, a few hundred kilometers from the active volcanic centers. This suggests again either higher temperature in the region and/or the presence of partial melt as might be expected for a region near a mantle plume.

5. Conclusion

We develop a method for joint inversion of ambient noise and teleseismic data for phase velocity maps using the two-plane wave teleseismic method.

We illustrate the utility of the inversion by applying it to data recorded in Iceland. The joint inversion allows all possible data to be used and satisfied in a self-consistent phase velocity model, rather than choosing one data set over another or averaging the different phase velocity maps where the period ranges overlap. We

illustrate the advantage of the joint inversion in checkerboard tests where the approach improves model recovery both inside and outside the array in comparison to using the data sets independently. The resulting phase velocity maps from the joint inversion are significantly different than those from approaches that consider only ambient noise, only teleseismic data, or a mean of the two. In addition, the joint inversion produces smoother dispersion curves at the edges of the Iceland array, for example, beneath the NW Fjords, and this improves the resulting 1-D shear velocity profiles.

Including ambient noise extends resolution to shallower depths and shorter periods in comparison to previous teleseismic studies beneath Iceland. We image similar structures to previous studies, but we also find low-velocity anomalies beneath the Reykjanes Ridge and Kolbeinsey Ridge consistent with the notion of mid-ocean ridge spreading. Future work will incorporate the joint inversion phase velocity maps into a 3-D shear velocity inversion for the region. In addition, longer-period ambient noise could be included at a location where station aperture is larger to extend the joint inversion to longer periods, which would further enhance the shear velocity inversion.

Acknowledgments
Seismic data used in this study were downloaded from the Incorporated Research Institutions for Seismology Data Management Center (http://ds.iris.edu/ds/nodes/dmc/). N. Harmon and C. Rychert were supported by the Natural Environment Research Council grants NE/M003507/1 and NE/K010654/1. We thank Kevin Ward and one anonymous reviewer for their helpful comments.

References

Aki, K., and P. G. Richards (2002), *Quantitative Seismology*, 2nd ed., 700 pp., Univ. Sci. Books, Sausalito, Calif.
Allen, R. M., et al. (1999), The thin hot plume beneath Iceland, *Geophys. J. Int.*, *137*(1), 51–63, doi:10.1046/j.1365-246x.1999.00753.x.
Allen, R. M., et al. (2002a), Imaging the mantle beneath Iceland using integrated seismological techniques, *J. Geophys. Res.*, *107*(B12), 2325, doi:10.1029/2001JB000595.
Allen, R. M., et al. (2002b), Plume-driven plumbing and crustal formation in Iceland, *J. Geophys. Res.*, *107*(B8), 2163, doi:10.1029/2001JB000584.
Asch, K. (2003), *The 1:5 Million International Geological Map of Europe and Adjacent Areas*, Schweizerbart, Stuttgart, Germany.
Bensen, G. D., M. H. Ritzwoller, M. P. Barmin, A. L. Levshin, F. Lin, M. P. Moschetti, N. M. Shapiro, and Y. Yang (2007), Processing seismic ambient noise data to obtain reliable broad-band surface wave dispersion measurements, *Geophys. J. Int.*, *169*, 1239–1260, doi:10.1111/j.1365-1246X.2007.03374.x.
Bird, P. (2003), An updated digital model of plate boundaries, *Geochem. Geophys. Geosys.*, *4*(3), 1027, doi:10.1029/2001GC000252.
Coffin, M. F., and O. Eldholm (1994), Large igneous provinces: Crustal structure, dimensions, and external consequences, *Rev. Geophys.*, *32*, 1–36, doi:10.1029/93RG02508.
Darbyshire, F. A., R. S. White, and K. F. Priestley (2000), Structure of the crust and uppermost mantle of Iceland from a combined seismic and gravity study, *Earth Planet. Sci. Lett.*, *181*(3), 409–428, doi:10.1016/S0012-821x(00)00206-5.
Forsyth, D. W., and A. Li (2005), Array-analysis of two-dimensional variations in surface wave phase velocity and azimuthal anisotropy in the presence of multipathing interference, in *Seismic Earth: Array Analysis of Broadband Seismograms*, *Geophys. Monogr. Ser.*, edited by A. Levander and G. Nolet, pp. 81–97, AGU, Washington, D. C.
Foulger, G. R., et al. (2000), The seismic anomaly beneath Iceland extends down to the mantle transition zone and no deeper, *Geophys. J. Int.*, *142*(3), F1–F5, doi:10.1046/j.1365-246x.2000.00245.x.
Hammond, W. C., and E. D. Humphreys (2000), Upper mantle seismic wave velocity: Effects of realistic partial melt geometries, *J. Geophys. Res.*, *105*, 10,975–10,986, doi:10.1029/2000JB900041.
Harmon, N., D. Forsyth, and S. Webb (2007), Using ambient seismic noise to determine short-period phase velocities and shallow shear velocities in young oceanic lithosphere, *Bull. Seismol. Soc. Am.*, *97*, 2024–2039.
Harmon, N., P. Gerstoft, C. A. Rychert, G. A. Abers, M. Salas de la Cruz, and K. M. Fischer (2008), Phase velocities from seismic noise using beamforming and cross correlation in Costa Rica and Nicaragua, *Geophys. Res. Lett.*, *35*, L19303, doi:10.1029/2008GL03587.
Harmon, N., D. W. Forsyth, and D. S. Weeraratne (2009), Thickening of young Pacific lithosphere from high-resolution Rayleigh wave tomography: A test of the conductive cooling model, *Earth Planet. Sci. Lett.*, *278*(1–2), 96–106.
Harmon, N., C. A. Rychert, and P. Gerstoft (2010), Distribution of noise sources for seismic interferometry, *Geophys. J. Int.*, *183*(3), 1470–1484, doi:10.1111/j.1365-246X.2010.04802.x.
Harmon, N., D. W. Forsyth, D. S. Weeraratne, Y. Yang, and S. C. Webb (2011), Mantle heterogeneity and off axis volcanism on young Pacific lithosphere, *Earth Planet. Sci. Lett.*, *311*(3–4), 306–315, doi:10.1016/j.epsl.2011.09.038.
Harmon, N., M. S. D. L. Cruz, C. A. Rychert, G. Abers, and K. Fischer (2013), Crustal and mantle shear velocity structure of Costa Rica and Nicaragua from ambient noise and teleseismic Rayleigh wave tomography, *Geophys. J. Int.*, *195*(2), 1300–1313, doi:10.1093/gji/ggt309.
Herrin, E., and T. Goforth (1977), Phase-matched filters—Application to study of Rayleigh-waves, *Bull. Seismol. Soc. Am.*, *67*(5), 1259–1275.
Jackson, I., and U. H. Faul (2010), Grainsize-sensitive viscoelastic relaxation in olivine: Towards a robust laboratory-based model for seismological application, *Phys. Earth Planet. Inter.*, *183*(1–2), 151–163, doi:10.1016/j.pepi.2010.09.005.
Kumar, P., R. Kind, K. Priestley, and T. Dahl-Jensen (2007), Crustal structure of Iceland and Greenland from receiver function studies, *J. Geophys. Res.*, *112*, B03301, doi:10.1029/2005JB003991.
Landisman, M., A. Dziewonski, and Y. Sato (1969), Recent improvements in the analysis of surface wave observations, *Geophys. J. R. Astron. Soc.*, *17*(4), 369–403.
Levshin, A. L., and M. H. Ritzwoller (2001), Automated detection, extraction, and measurement of regional surface waves, *Pure Appl. Geophys.*, *158*(8), 1531–1545, doi:10.1007/PL00001233.
Li, A. B., and R. S. Detrick (2004), Azimuthal anisotropy and phase velocity beneath Iceland: Implication for plume-ridge interaction (vol 214, pg 153, 2003), *Earth Planet. Sci. Lett.*, *218*(1–2), 241, doi:10.1016/S0012-821x(03)00633-2.
Li, A. B., and R. S. Detrick (2006), Seismic structure of Iceland from Rayleigh wave inversions and geodynamic implications, *Earth Planet. Sci. Lett.*, *241*(3–4), 901–912, doi:10.1016/j.epsl.2005.10.031.
Liang, C. T., and C. A. Langston (2009), Wave gradiometry for USArray: Rayleigh waves, *J. Geophys. Res.*, *114*, B02308, doi:10.1029/2008JB005918.
Lin, F. C., and M. H. Ritzwoller (2011), Helmholtz surface wave tomography for isotropic and azimuthally anisotropic structure, *Geophys. J. Int.*, *186*(3), 1104–1120, doi:10.1111/j.1365-246X.2011.05070.x.

Luo, Y. H., Y. J. Yang, Y. X. Xu, H. R. Xu, K. F. Zhao, and K. Wang (2015), On the limitations of interstation distances in ambient noise tomography, *Geophys. J. Int.*, *201*(2), 652–661, doi:10.1093/gji/ggv043.

Ma, Y. R., and R. W. Clayton (2014), The crust and uppermost mantle structure of Southern Peru from ambient noise and earthquake surface wave analysis, *Earth Planet. Sci. Lett.*, *395*, 61–70, doi:10.1016/j.epsl.2014.03.013.

Maclennan, J., D. McKenzie, and K. Gronvold (2001), Plume-driven upwelling under central Iceland, *Earth Planet. Sci. Lett.*, *194*(1–2), 67–82, doi:10.1016/S0012-821x(01)00553-2.

Martin, E., J. L. Paquette, V. Bosse, G. Ruffet, M. Tiepolo, and O. Sigmarsson (2011), Geodynamics of rift-plume interaction in Iceland as constrained by new $Ar-^{40}/Ar-^{39}$ and in situ U-Pb zircon ages, *Earth Planet. Sci. Lett.*, *311*(1–2), 28–38, doi:10.1016/j.epsl.2011.08.036.

Mordret, A., M. Landes, N. M. Shapiro, S. C. Singh, P. Roux, and O. I. Barkved (2013), Near-surface study at the Valhall oil field from ambient noise surface wave tomography, *Geophys. J. Int.*, *193*(3), 1627–1643, doi:10.1093/gji/ggt061.

Morgan, W. J. (1971), Convection plumes in the lower mantle, *Nature*, *230*, 42–43.

Nishida, K. (2011), Two-dimensional sensitivity kernels for cross-correlation functions of background surface waves, *C. R. Geosci.*, *343*(8–9), 584–590, doi:10.1016/J.Crte.2011.02.004.

Pollitz, F. F., and J. A. Snoke (2010), Rayleigh-wave phase-velocity maps and three-dimensional shear velocity structure of the western US from local non-plane surface wave tomography, *Geophys. J. Int.*, *180*(3), 1153–1169, doi:10.1111/j.1365-246X.2009.04441.x.

Porritt, R. W., R. M. Allen, and F. F. Pollitz (2014), Seismic imaging east of the Rocky Mountains with USArray, *Earth Planet. Sci. Lett.*, *402*, 16–25, doi:10.1016/j.epsl.2013.10.034.

Putirka, K. D., M. Perfit, F. J. Ryerson, and M. G. Jackson (2007), Ambient and excess mantle temperatures, olivine thermometry, and active vs. passive upwelling, *Chem. Geol.*, *241*(3–4), 177–206, doi:10.1016/j.chemgeo.2007.01.014.

Sabra, K. G., P. Gerstoft, P. Roux, W. A. Kuperman, and M. C. Fehler (2005), Surface wave tomography from microseisms in Southern California, *Geophys. Res. Lett.*, *32*, L14311, doi:10.1029/2005GL023155.

Saemundsson, K. (1974), Evolution of axial rifting zone in Northern Iceland and Tjornes fracture zone, *Geol. Soc. Am. Bull.*, *85*(4), 495–504.

Saito, M. (1988), DISPER80: A subroutine package for the calculation of seismic normal-mode solutions, in *Seismological Algorithms: Computational Methods and Computer Programs*, edited by D. J. Doornbos, pp. 293–319, Academic, San Diego, Calif.

Schilling, J. G. (1973), Iceland mantle plume—Geochemical study of Reykjanes Ridge, *Nature*, *242*(5400), 565–571, doi:10.1038/242565a0.

Schimmel, M., E. Stutzmann, and J. Gallart (2011), Using instantaneous phase coherence for signal extraction from ambient noise data at a local to a global scale, *Geophys. J. Int.*, *184*(494–506), 494–506.

Shapiro, N. M., and M. Campillo (2004), Emergence of broadband Rayleigh waves from correlations of the ambient seismic noise, *Geophys. Res. Lett.*, *31*, L07614, doi:10.1029/2004GL019491.

Shapiro, N. M., M. Campillo, L. Stehly, and M. H. Ritzwoller (2005), High-resolution surface-wave tomography from ambient seismic noise, *Science*, *307*(5715), 1615–1618.

Shen, Y., S. C. Solomon, I. T. Bjarnason, and C. J. Wolfe (1998), Seismic evidence for a lower-mantle origin of the Iceland plume, *Nature*, *395*(6697), 62–65, doi:10.1038/25714.

Tarantola, A., and B. Valette (1982), Generalized nonlinear inverse problems solved using the least squares criterion, *Rev. Geophys.*, *20*, 219–232, doi:10.1029/RG020i002p00219.

Tromp, J., Y. Luo, S. Hanasoge, and D. Peter (2010), Noise cross-correlation sensitivity kernels, *Geophys. J. Int.*, *183*(2), 791–819.

Venzke, E. (Ed.) (2013), *Global Volcanism Program*, The Smithsonian Inst., Washington, D. C., doi:10.5479/si.GVP.VOTW4-2013.

Vogt, P. R. (1976), Plumes, subaxial pipe-flow, and topography along mid-oceanic ridge, *Earth Planet. Sci. Lett.*, *29*(2), 309–325, doi:10.1016/0012-821x(76)90135-7.

Weeraratne, D. S., D. W. Forsyth, Y. Yang, and S. C. Webb (2007), Rayleigh wave tomography beneath intraplate volcanic ridges in the South Pacific, *J. Geophys. Res.*, *112*, B06303, doi:10.1029/2006JB00440.

Wilson, J. T. (1965), Convection currents and continental drift, *Trans. R. Soc.*, *258*(19), 145–167.

Wolfe, C. J., I. T. Bjarnason, J. C. VanDecar, and S. C. Solomon (1997), Seismic structure of the Iceland mantle plume, *Nature*, *385*(6613), 245–247, doi:10.1038/385245a0.

Yang, Y., and D. W. Forsyth (2006), Regional tomographic inversion of amplitude and phase of Rayleigh waves with 2-D sensitivity kernels, *Geophys. J. Int.*, *166*(3), 1148–1160.

Yang, Y., D. W. Forsyth, and D. S. Weeraratne (2007), Seismic attenuation near the East Pacific Rise and the origin of the low-velocity zone, *Earth Planet. Sci. Lett.*, *258*(1–2), 260–268.

Yang, Y., M. H. Ritzwoller, F. C. Lin, M. P. Moschetti, and N. M. Shapiro (2008), The structure of the crust and uppermost mantle beneath the western US revealed by ambient noise and earthquake tomography, *J. Geophys. Res.*, *113*, B12310, doi:10.1029/2008JB005833.

Yang, Y. J. (2014), Application of teleseismic long-period surface waves from ambient noise in regional surface wave tomography: A case study in western USA, *Geophys. J. Int.*, *198*(3), 1644–1652, doi:10.1093/gji/ggu234.

Zhou, L. Q., J. Y. Xie, W. S. Shen, Y. Zheng, Y. J. Yang, H. X. Shi, and M. H. Ritzwoller (2012), The structure of the crust and uppermost mantle beneath South China from ambient noise and earthquake tomography, *Geophys. J. Int.*, *189*(3), 1565–1583, doi:10.1111/j.1365-246X.2012.05423.x.

Zhou, Y., F. A. Dahlen, and G. Nolet (2004), Three-dimensional sensitivity kernels for surface wave observables, *Geophys. J. Int.*, *158*(1), 142–168.